TUTORIAL

Generalized Sheet Transition Conditions (GSTCs) in Electromagnetic Metasurface Modeling

ALIREZA GHANEIZADEH AND MOJTABA JOODAKI, (Senior Member, IEEE)

School of Computer Science and Engineering, Constructor University, 28759 Bremen, Germany

Corresponding author: Mojtaba Joodaki (mjoodaki@constructor.university)

ABSTRACT We present a modeling framework for metasurfaces illuminated by a plane wave based on the Generalized Sheet Transition Conditions (GSTCs). This framework describes how conventional boundary conditions are converted to GSTCs. In order to provide a physical insight into the induced dipole moments of simple small scatters, different snapshots are used when the maximum electric or maximum magnetic field touches the metasurface. The spatial derivatives of the normal components of the induced surface polarization densities are physically justified by considering all possible cases. It is shown that both the normal and transverse components of the electric surface polarization density and surface magnetization (magnetic polarization) density should be included in studying the most general case in the metasurface. In addition, we have reviewed three different modeling approaches for describing the GSTCs, which are polarizability, susceptibility, and impedance/admittance models. The interrelations between these approaches are also discussed. Finally, we have reviewed the generalized modeling approaches of GSTCs for synthesizing bianisotropic metasurfaces via all three mentioned models. This review provides several examples to demonstrate how to design a desired metasurface using GSTCs. This tutorial study may open new paradigms for a better modeling and conceptual understanding of GSTCs.

INDEX TERMS Boundary conditions, dipole moment, generalized sheet transition conditions, GSTCs, metasurface.

I. INTRODUCTION

Electromagnetic waves, from radio waves to X-rays, form the backbone of most of modern infrastructures and technologies. However, when electromagnetic waves generated by time-varying current or charge distributions encounter electromagnetic discontinuities in a propagation medium, they can exhibit complex behaviors. Understanding and analyzing these effects is essential to comprehend the behavior of electromagnetic waves. In the macroscopic domain, Maxwell's equations can determine the wave responses. In order to solve Maxwell's equations, permeability (μ), permittivity (ε) and conductivity (σ) are the only three macroscopic constitutive parameters of the material media needed to describe the relationships between macroscopic field quantities [1]. These parameters for an ordinary medium

The associate editor coordinating the review of this manuscript and approving it for publication was Derek Abbott.

are only scalar values, which means they are isotropic, time-invariant, linear and homogeneous. However, these parameters for a complex medium (i.e., anisotropic, time-variant, non-linear or inhomogeneous medium) may depend on orientations of the magnetic and electric fields (anisotropic), time (time-variant), magnitudes of the magnetic and electric fields (non-linear), or location (inhomogeneous) [1].

In order to control the phase, amplitude, and polarization of the electromagnetic wave, specific materials are often employed [2]. Unfortunately, ordinary materials have particular ranges of μ and ε, which limits their electromagnetic responses. In fact, electromagnetic properties of the materials derived from the periodic table of elements are in a specific range of values associated with various factors, e.g., the operation frequency [2]. This limitation of the ordinary material leads to the restriction of wave-matter interaction. To overcome this physical limitation,

the artificially engineered metamaterials, which are three-dimensional (3D), generate opportunities for researchers in both physics and engineering communities to extend the range of effective μ and ε values beyond what nature has provided to us [2], [3], [4], and [5]. Meta-structures are engineered composites of (periodically or non-periodically) sub-wavelength polarizable artificial particles, which are called meta-atoms [4], [5], [6], [7], [8], [9], [10], [11], [12], [13].

The subwavelength meta-atoms, scattering particles of metamaterial often periodically embedded in a host medium, can be designed in different ways, resulting in extreme wave manipulation performance [2], [6], [7], [8], [9], [10], [11], [12], [13]. Due to the lower loss, profile size and several fabrication challenges of voluminal metamaterials, the two-dimensional counterparts, or planar versions of the metamaterials, termed metasurfaces, with subwavelength thickness are often employed. The metasurfaces are artificial electromagnetic surfaces whose thickness is infinitesimal in comparison with the operating wavelength [2], [6], [7], [8], [9], [10], [11], [12], [13], [14].

Dipolar approximations are the basis of most of the modeling and design techniques used for the analysis and synthesis of metasurfaces [15]. This is due to the fact that the polarizable scattering particles which compose the metasurfaces are sufficiently small in comparison with the operating wavelength [15]. In such a case, the surface creates dipole moment responses when it is impinged by the electromagnetic wave-front [16], [17], [18]. Therefore, the meta-atoms can be considered as induced electric and/or magnetic dipole moments that are dependent on the local electric and magnetic fields through polarizability (or susceptibility) tensors [9], [10], [11], [12], [13], [19]. In fact, metasurfaces are broadly employed for their powerful synthesis techniques [20], offering an unprecedented opportunity to manipulate fundamental properties of electromagnetic waves, including phase, amplitude, and polarization [2], [7]. These capabilities lead to a myriad of electromagnetic applications which have been demonstrated for various functionalities in recent years, e.g., metasurface magnetless specular isolators [20], flexible metasurface energy harvesters [21], metasurface antennas [22], and holographic metasurfaces [23] to name a few. Different examples of metasurface structure cells in the microwave regime and THz-optical frequency ranges [24], [25], [26] are shown in Fig. 1 and Fig. 2, respectively. In addition, the metasurface structures can be either fixed or made reconfigurable by implementing electronic devices such as pin diodes, varactor diodes and transistors [27], [28].

This review paper provides a comprehensive tutorial on Generalized Sheet Transition Conditions (GSTCs), which are commonly used in modeling and designing metasurfaces. The aim of the paper is to explain GSTCs in a simple manner and discuss various synthesis approaches, such as impedance, polarizability, and susceptibility, that are typically employed in metasurface design. This paper will also review three synthesis approaches for bianisotropic metasurfaces, considering both magneto-electric and electro-magnetic coupling coefficients. Finally, several simple examples will be reviewed to demonstrate how GSTCs can be effectively used in metasurface design. The main goal of this paper is to serve as a foundational resource for researchers in this field who wish to conceptually understand the metasurface boundary conditions.

To this end, the rest of the paper is organized as follows. Section II presents the metasurface synthesis problem, showcasing GSTCs as a potent synthesis technique which can be integrated into different numerical methods, thereby enhancing the simulation design speed of metasurface structures. Section III briefly surveys the fundamental concepts of Maxwell's equations and the conventional boundary conditions. Subsequently, Section IV demonstrates how the conventional boundary conditions are transformed to GSTCs. Section V reviews various modeling approaches for characterizing GSTCs. Section VI focuses on bianisotropic metasurface structures. Section VII reviews examples of designed metasurface structures employing different GSTC modeling approaches, and finally, the paper is concluded in Section VIII.

II. METASURFACE SYNTHESIS PROBLEM

The conventional theory of effective medium or "modified" Nicolson-Ross-Weir (NRW) technique is known to be a useful approach to model bulk metamaterial properties [13], [29], [30]. However, in many investigations, researchers have proven that the theory is impractical to parametrize the metasurfaces (as their 2D version) [13]. In practice, the extracted bulk parameters of a metasurface - i.e., permittivity (ε) and permeability (μ) - are affected by its thickness [13], [16], [17]. In addition, conventional metamaterial modeling is challenged when the thickness of metamaterial is extremely small in comparison with the incident wavelength [13]. For example, the Kramers-Kroning relations that join the real and imaginary parts of (μ) and (ε) may be contravened so that a passive material may demonstrate the features of a non-passive material (i.e., non-physical behaviors), reviewed in detail in [13]. As the second example, the admittance (or impedance) boundary condition as $\Delta \mathbf{H} = \overline{\overline{Y}} \cdot \mathbf{E}$ ($\Delta \mathbf{E} = \overline{\overline{Z}} \cdot \mathbf{H}$) also fails to explain some metasurfaces since the admittance (or impedance) boundary condition can assume a discontinuity in either $\mathbf{E}$ or $\mathbf{H}$ [12]; where $\overline{\overline{Y}}$ and $\overline{\overline{Z}}$ are defined as surface admittance and impedance tensors, related to the magnetic and electric discontinuities, respectively [12]. The Δ operator is the difference between the vectorial fields on both sides of the interface. Besides, the right-hand side fields ($\mathbf{E}$ and $\mathbf{H}$) in equations of the admittance (or impedance) boundary condition denote the average fields on either side of the interface. For simplicity of notation, throughout this paper, we will employ $\Delta \mathbf{E}$ and $\Delta \mathbf{H}$, which refer to the difference between the vector components of the electric and magnetic fields, respectively. In fact, the
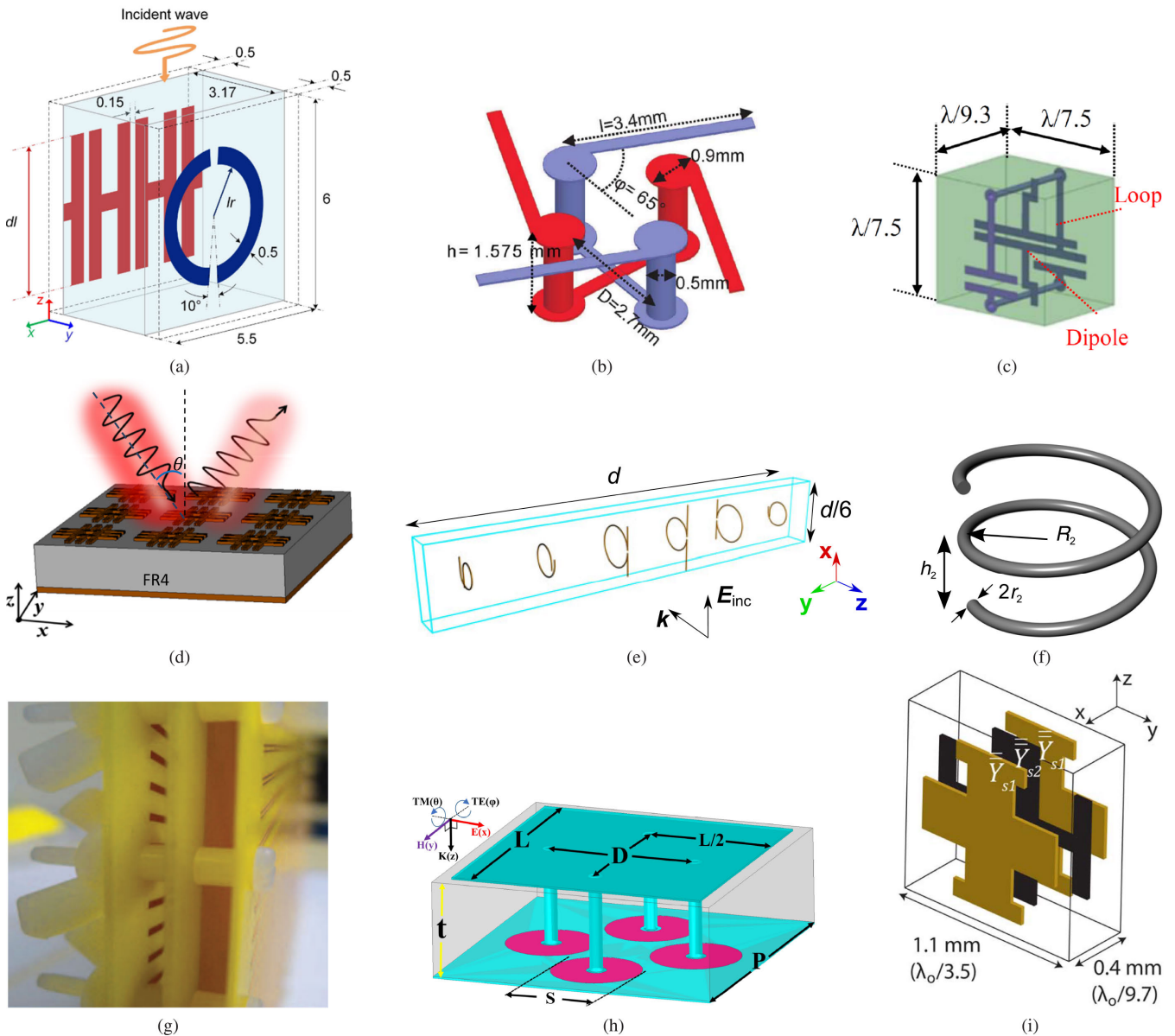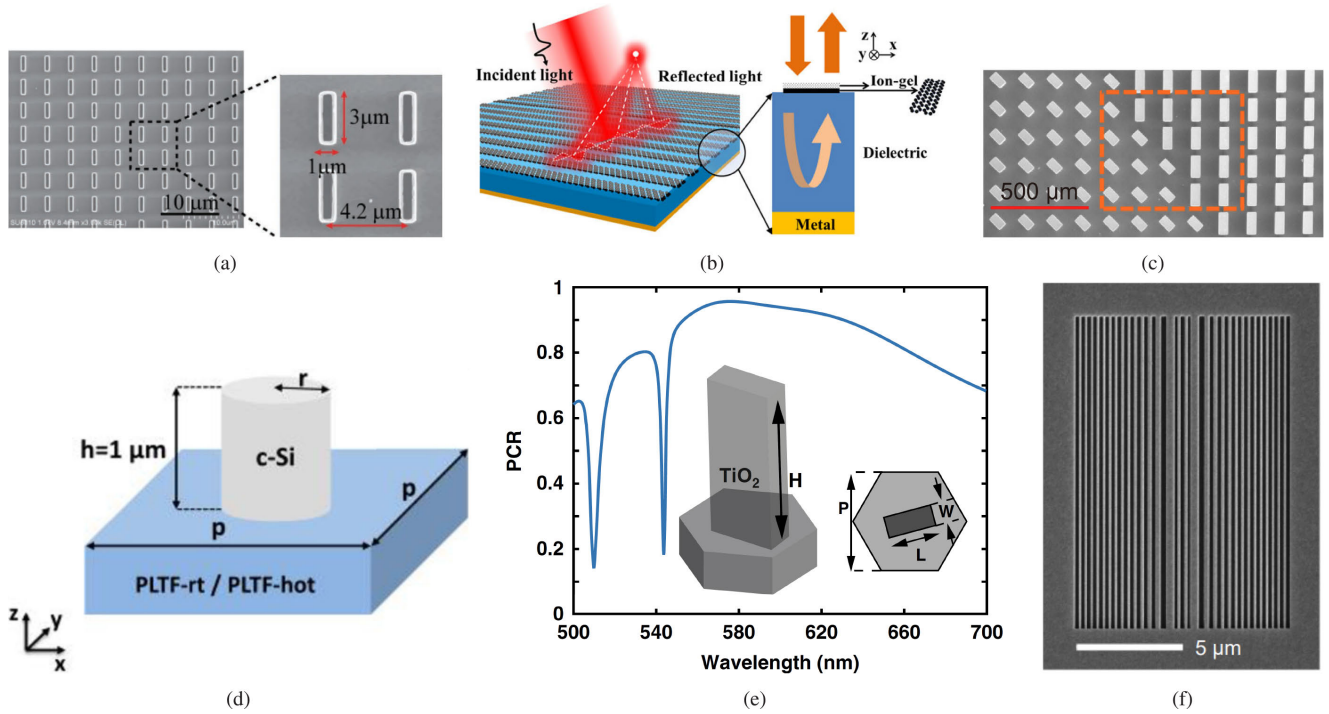
FIGURE 1. Examples of metasurface structure's cell in the microwave regime. (a) The designed wire-loop unit cell (unit: mm) [33], (b) polarization-sensitive unit cell realized with modifying chiral elements on a PCB [34], (c) longitudinal wire-loop unit cell [35], (d) metasurface absorber constructed using split-ring resonators (SRR) encircled by an E-shaped fractal structure [36], (e) The period of a metasurface mirror comprises of 6 subwavelength metallic omega-shaped cells Reprinted figure with permission from [37] Copyright (2015) by the American Physical Society, (f) helix-shaped unit-cell Reprinted from [38], licensed under a Creative Commons Attribution 3.0 License, (g) a picture of the three stacked layers of the fabricated circular polarization selective surface [39], (h) the electromagnetic energy harvester unit-cell [32], and (i) three stacked layers unit cell [40].

metasurface boundary conditions are often more enhanced than the conventional boundary conditions, e.g., boundary conditions of Huygens's metasurface.

It should be noted that the analysis and design of metasurface structures are usually performed by using different commercial simulation software, such as COMSOL, CST, FEKO, Lumerical and HFSS based on different numerical methods, including Finite Element Method (FEM), Finite Difference Time Domain (FDTD), Method of Moments (MoM), etc. Furthermore, the design of electromagnetic devices based on a "cut-and-try" operation [31] or time-consuming

optimization procedures guiding by engineering experiences and/or metaheuristic approaches may be laborious work [32], particularly when the electromagnetic devices have become a complex-shaped structure with different loads and irregular discontinues, etc. For example, Fig. 3 shows the electric field distribution simulation results on a metasurface energy harvester designed in [6]. Notably, this metasurface array is excited by a normal incident plane wave at its resonance frequency (10 GHz) to generate the desired surface current densities. As shown in this figure, the electric field has got a non-uniform distribution on each cell over a small distance

FIGURE 2. Examples of metasurface structure's cell in the THz, infrared and optical frequency ranges. (a) Scanning electron microscope (SEM) images showcasing the manufactured metasurface antenna, featuring a periodicity of 4.2 μm, a length of 1 μm, and a width of 3 μm. The design is tailored for operation at a wavelength (λ) of 9.6 μm Reprinted from [41], licensed under a Creative Commons Attribution license. (b) The image of a tunable metasurface lens with an array of ion-gel layers and graphene ribbons, along with a metallic reflector, and a dielectric spacer [42], (c) SEM image of a fabricated metasurface structure designed to convert arbitrary polarizations into a fixed polarization within the THz frequency range reprinted from [43] licensed under a CC BY license, (d) a three-dimensional schematic showing a designed thermally tuning infrared unit cell, which includes a cylindrical post made of crystal silicon (c-Si) positioned on the tunable planar layered thin film (PLTF) structure [44], (e) A schematic view of a hexagonally-shaped unit cell, consisting of TiO2 nanopillars on a SiO2 substrate, along with the corresponding results for its polarization conversion ratio (PCR) across different wavelengths reprinted from [45] licensed under the Creative Commons CC BY license, where W =100 nm, L =240 nm, P = 300 nm, and H = 800 nm. (f) An SEM image captures the manufactured metasurface superlens working under 405 nm illumination Reprinted from [46] licensed under a CC BY license.

compared to the incident wavelength from the metasurface plane [6]. The reason behind these field distributions is the interaction between the incident plane-wave and the metasurface structure to create the proper scattered wave for electromagnetic energy harvesting. For the sake of clarity, Fig. 4 shows how the distribution of the real Poynting vectors redirect themselves with minimum reflections towards the edges of an illuminated cell of metasurface energy harvester at 5.82 GHz designed in [32]. The purpose of these two case studies is to show that developing a metasurface structure for manipulating the electromagnetic wave may incur a tedious and time-consuming process based on the simulation approaches.

Recently, researchers are trying to use the GSTCs to characterize the metasurface [8], [9], [11], [12], [16], [47], [48], [49]. However, some examples are given in [48], demonstrating that the direct calculation of unknown susceptibilities, which are heavily underdetermined, is not possible only using the GSTCs equations. Because of the difficulty in finding the exact field quantities at the metasurface boundary, some simplifications or approximations are needed [19]. Some methods for implementing these simplifications and

calculation of the tensors are presented in [48]. Although, to our best knowledge, there is no commercial electromagnetic software on the market using GSTCs [50], [51], different numerical methods have employed GSTCs for electromagnetic simulation of metasurfaces, e.g., the discontinuous Galerkin time-domain (DGTD) in [50] and [51], the finite difference time-domain (FDTD) in [12] and [52], the finite-element method (FEM) in [53], the finite difference frequency-domain (FDFD) in [54], the spectral-domain integral equations (SD-IEs) in [55], the multifilament current (MFC) in [56], the IE-based method of moments (IE-MoM) in [57]. In [50], for example, they introduced the "virtual edges" after and before the metasurface to incorporate the DGTD method on GSTCs (see Fig. 1 in [50]). Besides, multiple representative simulation examples to validate the effectiveness of the mentioned numerical methods, incorporating GSTCs have been presented and benchmarked in the literature. Motivated by the interesting opportunities that GSTCs can provide, in this paper we elaborate on the physical justification of GSTCs using the basic Maxwell's equations that have already been studied in detail in [9], [12], [13], [19], [48], and [58].
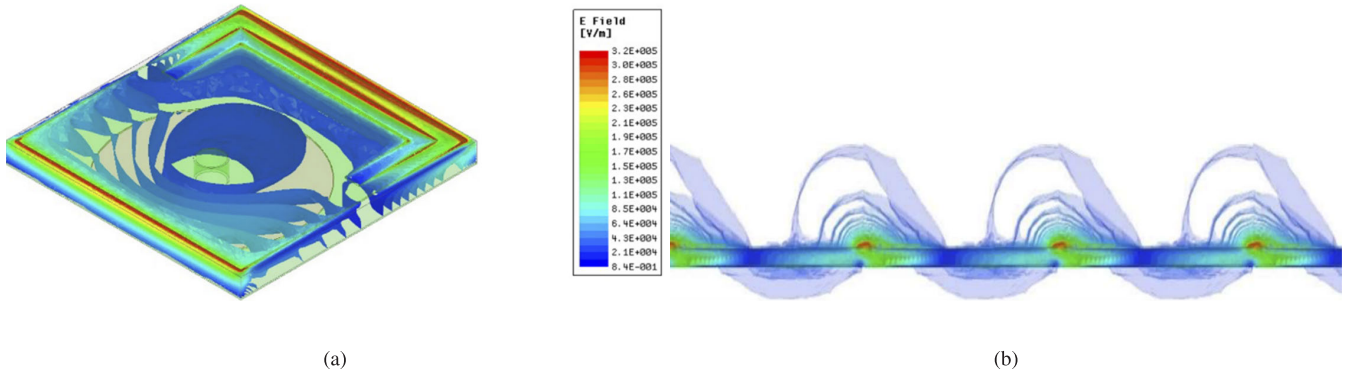
FIGURE 3. The electric field distribution over the metasurface energy harvester unit cells illuminated by a normal incident plane wave at 10 GHz. (a) a 3D perspective view of the induced electric field on a unit-cell Reprinted from [6], licensed under a Creative Commons Attribution (CC BY) license and (b) a side view of the induced electric field on a row of unit cells Reprinted from [6], licensed under a Creative Commons Attribution (CC BY) license.
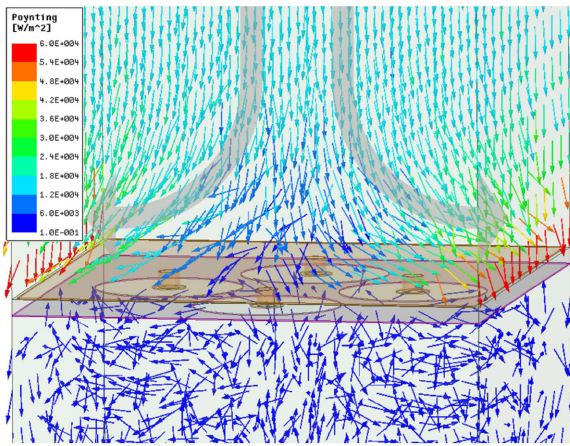
FIGURE 4. A 3D perspective view of real Poynting vector distribution induced over a unit-cell with a thickness of 0.254 mm at 5.82 GHz [32].

III. BACKGROUND
In this section, we briefly review the fundamental concepts of Maxwell's equations and the conventional boundary conditions, which are essential for a better understanding of the generalized surface transition conditions.

A. FUNDAMENTAL CONCEPTS
Generally, the reaction of a medium to an applied electromagnetic field can be described by the responses of the atomic dipole moments (electric and magnetic) and displacement of both bounded and unbounded charges [1], [59]. From an electromagnetic point of view, this medium contains polarizable scattering particles and the vacuum space between them, each having individual responses to electromagnetic waves. The scattering particles responses typically include electric and magnetic polarization densities (**P** and **M**), while the vacuum space responses involve $\varepsilon_0 \mathbf{E}$ and $\mu_0 \mathbf{H}$ [10]. Furthermore, these particles may be induced by both electric and magnetic vector fields and may exhibit electric/magnetic mutual couplings similar to particles in

bi-anisotropic materials [8], [38], [47], [60]. However, responses of most media are typically formulated by the electric (electric displacement field or electric flux density field) and magnetic (or magnetic flux density) vector fields of **D** and **B** as follows [1], [59], [61], [62], [63], [64]:

$$\mathbf{D} = \varepsilon_0 \mathbf{E} + \mathbf{P} \tag{1}$$
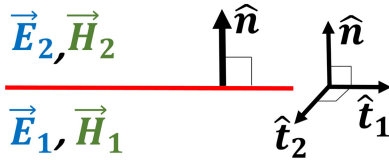
$$\mathbf{B} = \mu_0 \mathbf{H} + \mu_0 \mathbf{M} \tag{2}$$

where μ_0 and ε_0 are the free space permeability and permittivity, respectively. **P** ($\mu_0 \mathbf{M}$) is the response of the polarizable scattering particles from polarization material to the electromagnetic waves in the vector terms of electric (magnetic) polarization density. In addition to this, the term $\varepsilon_0 \mathbf{E}$ ($\mu_0 \mathbf{H}$) would be a contribution from the response of the vacuum between the polarizable scattering particles which have a **P** ($\mu_0 \mathbf{M}$) response [47], [59], [62], [63], [64], [65]. Actually, these particles are discretely polarized; however it is convenient to assume that the equivalent infinitesimal dipoles have a continuous distribution [59], [63], [64]. Based on the uniqueness theorem, two curl equations of Maxwell are required to determine the fields uniquely [9], [59], [62], [63], [64] as follows:

$$\nabla \times \mathbf{E} = -\frac{\partial \mathbf{B}}{\partial t} \tag{3}$$

$$\nabla \times \mathbf{H} = \frac{\partial \mathbf{D}}{\partial t} + \mathbf{J} \tag{4}$$

where **J** is the electric current density. In (3) and (4), the units of **E**, **H**, **D**, **B**, ε_0, and μ_0 are [V/m], [A/m], [C/m^2], [Wb/m^2], [F/m], and [H/m], respectively. At the interface discontinuity, it is convenient to solve Maxwell's equations in the integral form [59], [62], [63], [64]. Faraday's induction law and Ampere-Maxwell law in the integral forms are as follows:

$$\oint_C \mathbf{E} \cdot d\mathbf{l} = -\frac{\partial}{\partial t} \iint_S \mathbf{B} \cdot d\mathbf{s}$$

$$= -\frac{\partial}{\partial t} \iint_S (\mu_0 \mathbf{H} + \mu_0 \mathbf{M}) \cdot d\mathbf{s} \tag{5}$$

FIGURE 5. In the simplest model of showing the interface between two different media with two unit tangent vectors $\hat{t}_1$ and $\hat{t}_2$, and a normal unit vector $\hat{n}$, adapted from [8] licensed under a Creative Commons Attribution (CC BY) license.

$$\oint_C \mathbf{H} \cdot d\mathbf{l} = \frac{\partial}{\partial t} \oiint_S \mathbf{D} \cdot d\mathbf{s} + \oiint_S \mathbf{J} \cdot d\mathbf{s}$$
$$= \frac{\partial}{\partial t} \oiint_S (\varepsilon_0 \mathbf{E} + \mathbf{P}) \cdot d\mathbf{s} + \oiint_S \mathbf{J} \cdot d\mathbf{s} \quad (6)$$

where C and S are the abbreviations for the closed path (contour) and the surface containing the contour, respectively.

B. CONVENTIONAL BOUNDARY CONDITIONS

Traditionally, the two main boundary conditions derived by applying Stokes's theorem to Faraday's induction law and Ampere-Maxwell's law are as follows [59], [62], [63], [64]:

$$\hat{\mathbf{n}} \times (\mathbf{E}_2 - \mathbf{E}_1) = 0 \quad (7)$$
$$\hat{\mathbf{n}} \times (\mathbf{H}_2 - \mathbf{H}_1) = \mathbf{J}_s \quad (8)$$

where $\hat{\mathbf{n}}$ is the unit vector normal to the interface, and the magnetic and electric fields distributed on both sides of the interface are shown in Fig. 5 by $\mathbf{H}_1$ ($\mathbf{H}_2$) and $\mathbf{E}_1$ ($\mathbf{E}_2$). Besides, the tangent unit vectors are depicted by $\hat{t}_1$ and $\hat{t}_2$ in this figure. $\mathbf{J}_s$ is the surface current density, expressed in the unit of [A/m] [1], [59], [62], [63], [64]. In most metasurface applications, there is no $\mathbf{J}_s$ [66].

## IV. HOW CONVENTIONAL BOUNDARY CONDITIONS ARE CONVERTED TO GSTCS

Some metasurfaces, such as Huygens surfaces, exhibit bi-anisotropic behavior [60], [67], which cannot be fully described by (7) and (8). In fact, metasurfaces are interfaces that contain polarizable scattering particles across the interface. When the Stokes theory is applied to the metasurface by a rectangular contour, as shown in Fig. 6 and Fig. 7, it becomes clear that the responses of the vacuum space to electromagnetic waves, denoted by $\varepsilon_0 \mathbf{E}$ and $\mu_0 \mathbf{H}$, become zero at the interface. This occurs because the flux of fields passing through the Stokes rectangular tends towards zero as the rectangle's height diminishes to zero. However, metasurfaces can have yet induced electric and magnetic surface polarization densities that are parallel to the surface [12], [13], [15], [16], [17], [18], [19], [59], [63]. These tangential components of electric and magnetic surface polarization densities ($\mathbf{P}_\parallel$ and $\mu_0 \mathbf{M}_\parallel$) can be induced (resonated) by time-varying electromagnetic fields across the metasurface, resulting in the equivalent surface polarization current densities shown in Fig. 6 and Fig. 7. In Sections IV and V, we have assumed that there is no magneto-electric or
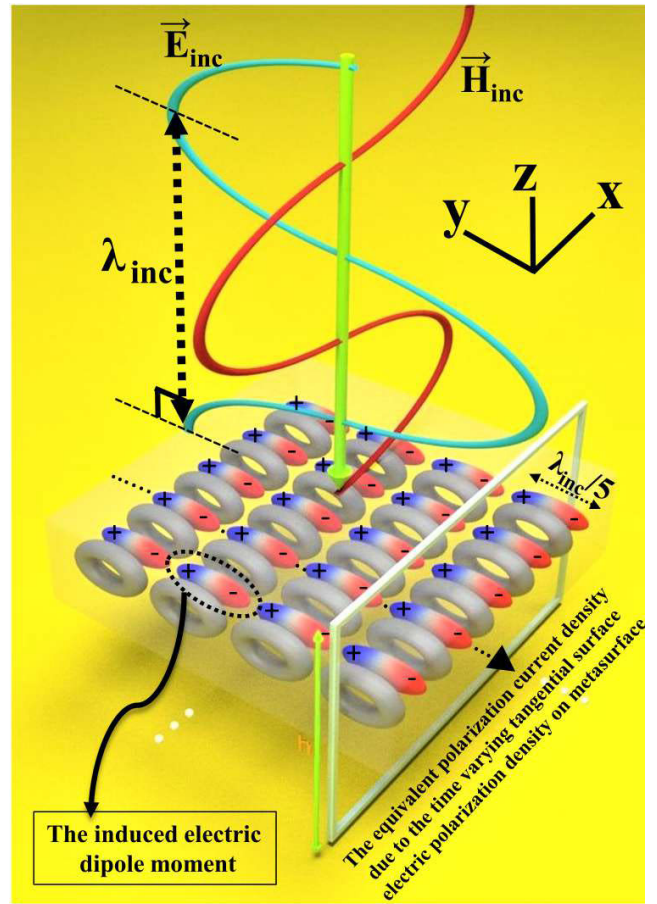
FIGURE 6. A schematic picture of a piece of a Huygens metasurface in the balance conditions when a normal incident plane wave at a resonance frequency of the metasurface illuminates it. This snapshot is shown when the maximum electric field touches the metasurface, resulting in the maximum exciting level of the tangential electric surface polarization density ($P_\parallel$) shown by the color capsules. Note that the gray doughnuts mean that the tangential magnetic surface polarization density ($M_\parallel$) is at its minimum exciting level. The metasurface sample is transparent.

electro-magnetic couplings between the meta-atoms, and the Huygen's metasurfaces are in a balanced condition. In fact, the balance condition mentioned in the captions of these figures refers to the balance condition between the magnetic and electric surface polarizabilities. This condition ensures that the magnetic and electric surface current densities induced in meta-atoms are equivalent, as they are responses of magnetic and electric moments to incident waves [32], [67], [68], [69]. Achieving this balance condition in Huygen's metasurface requires a careful design of the resonance characteristics of magnetic and electric dipoles at a specific frequency [8], [32], [67], [68], [69].

Basically, as long as there is no charge movement, the charge complies with electrostatic rules. Also, the charge complies with the magnetostatic laws if it moves with a constant velocity. However, according to Maxwell's equations, when an electric or magnetic field is time-varying, these two fields become interconnected. As a result, the polarizable scattering particles and their mutual interactions
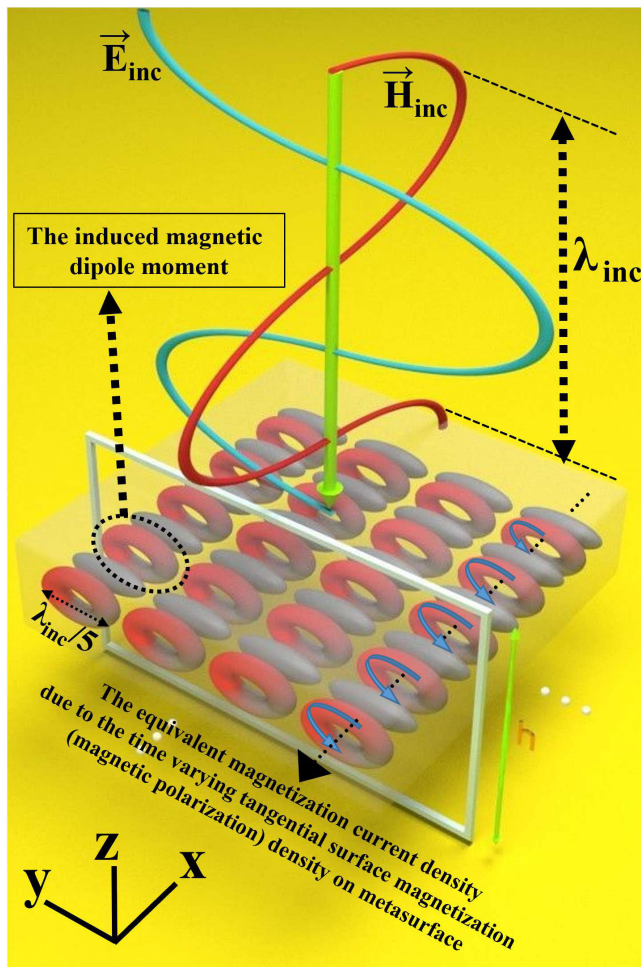
FIGURE 7. A schematic picture of a piece of a Huygens metasurface in the balance conditions when it is illuminated by a normal incident plane wave at the resonance frequency of metasurface. This snapshot is shown when the maximum magnetic field touches the metasurface, resulting in the maximum exciting level of tangential magnetic surface polarization densities ($M_\parallel$) shown by the colored doughnuts. The gray capsules mean the tangential electric surface polarization density ($P_\parallel$) is at its minimum exciting level. The metasurface sample is transparent.

become time-varying when excited by external electromagnetic waves, creating surface displacement currents. These displacement current densities can induce additional fields, which are then added to (7) and (8), as shown in (9) and (10).

For example, a study conducted in 2011 [70] demonstrated the generalized Snell's law of reflection and refraction. This generalized law can describe how phase discontinuity along the metasurface interface responds to incident plane waves. This law can address spatial gradient phase changes of the metasurface, as depicted in a simplified manner in Fig. 8. Over the years, there have been exponential improvements in the performance of metasurface structures, which has enabled the realization of various microwave, terahertz, and optical functions [10], [11], [12], [13], [15], [71].

Equations (9) and (10) introduce additional currents induced by the tangential component of electric and magnetic

surface polarization densities. These currents are added to the conventional boundary conditions because metasurfaces, as interfaces, can have tangential displacement currents associated with the tangential components of electric and magnetic surface polarization densities. These currents play a crucial role in the behavior of metasurfaces and need to be considered to model their electromagnetic response accurately.

Based upon Faraday's law, electromotive-force (emf) can be created around a loop due to the time-varying magnetic flux passing through it. According to Lens's law, this force is constructed around the loop in such a way that it opposes the magnetic flux variation. In the case of a metasurface, we would be able to observe the contribution of emf when a time-varying magnetic flux passes through a closed path shown as magnetic small scatters in Fig. 7. Additionally, in accordance with Ampere-Maxwell's law, the magnetomotive force (mmf) is equivalent to the total current going through the loop [59], [62], [63], [64]. Accordingly, the results of (5) and (6) for metasurfaces are summarized as follows:

$$\hat{\boldsymbol{n}} \times (\boldsymbol{E}_2 - \boldsymbol{E}_1) = -\mu_0 \frac{\partial \boldsymbol{M}_\parallel}{\partial t} \qquad (9)$$

$$\hat{\boldsymbol{n}} \times (\boldsymbol{H}_2 - \boldsymbol{H}_1) = \boldsymbol{J}_\text{s} + \frac{\partial \boldsymbol{P}_\parallel}{\partial t} \qquad (10)$$

In some cases, it is also possible that surface polarizable scattering particles with a non-uniform distribution are located in the metasurface plane in a way that their normal components of the electric surface polarization density and/or the surface magnetization (magnetic polarization) density are induced by a plane wave incident. However, only the ones whose spatial tangential gradient vector's direction is parallel to the interface may directly affect the tangential field discontinuity across the metasurface, as shown in Fig. 9 and Fig. 10.

Although the uniform distribution of the induced normal electric surface polarization density vectors does not affect the tangential components of electric fields (i.e., they have no spatial variation in the direction of the tangential components of the fields), it is crucial to consider the concept of electric surface polarizability, which involves the accumulation of electric charges. A non-uniform distribution of charge accumulation on the metasurface generates a tangential electric field, which influences the tangential field components.

In other words, this non-uniform charge distribution results in a non-zero tangential gradient of induced normal polarization density that is aligned with the tangential component of the field on the surface. This charge distribution directly impacts the discontinuity of the tangential electric field components, which is further explained in Fig. 11. For this reason, (9) must incorporate the tangential gradient of the induced normal polarization density. Similarly, (10) must include the tangential gradient of the induced normal magnetic surface polarization density. It should be mentioned
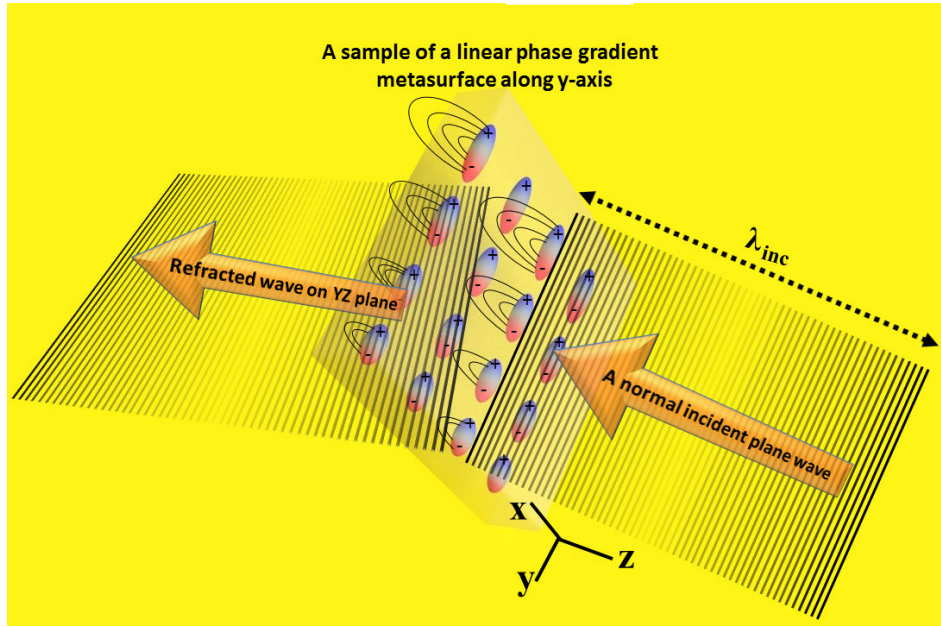
FIGURE 8. A schematic picture of a piece of a metasurface with a linear phase gradient along the y-axis illuminated by a normal incident plane wave in z-direction. Note that the meta-atoms' shape, geometry, and arrangement are designed so that each meta-atom row senses the incident wave by a different phase delay. The sizes of the colored capsules represent the electric surface polarization density ($P_\parallel$).
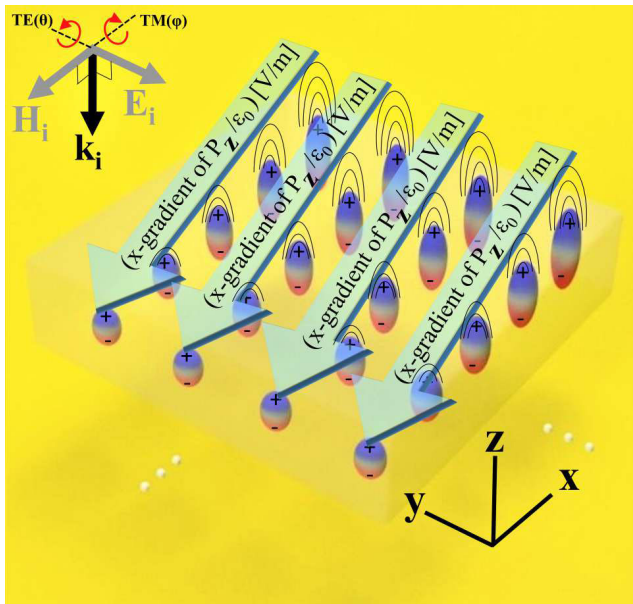
FIGURE 9. A schematic picture of a piece of a metasurface with the normal electric surface polarization densities illuminated by an incident plane wave. Note that the meta-atoms' shape, geometry, and arrangement are designed so that each meta-atom column senses the incident plane wave. The sizes of the colored capsules represent the normal electric surface polarization density (P_n). The spatial tangential gradient of these normal electric surface polarization densities can directly affect the discontinuity of the tangential components of electric fields on both sides of the metasurface.
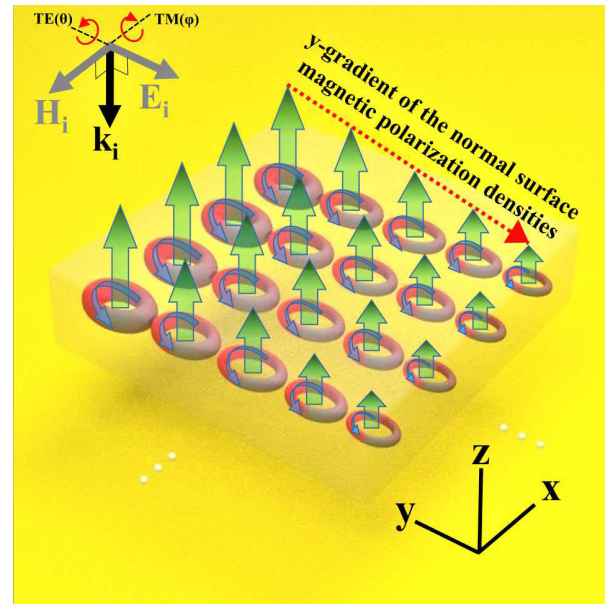
FIGURE 10. A schematic picture of a piece of a metasurface illuminated by an incident plane wave. Note that the meta-atoms' shape, geometry, and arrangement are designed so that each meta-atom column senses the incident plane wave. The sizes of the colored doughnuts represent the normal magnetic surface polarization density (M_n). The spatial tangential gradient of these normal magnetic surface polarization densities can directly affect the discontinuity of the tangential components of the magnetic fields on both sides of the metasurface.

that, as shown in Fig. 9 and Fig. 10, TE and TM waves are the two simplest propagation waves, and it is assumed that there are no electro-magnetic and magneto-electric coupling effects between the simple induced polarizable scatters.

The GSTCs connect the tangential electric and magnetic field discontinuities across the metasurface to the normal and tangential surface polarization densities. It is, therefore, convenient to decompose the magnetic and electric surface densities into normal (M_n and P_n) and tangential ($M_\parallel$ and $P_\parallel$) surface polarization densities to the metasurface plane [48].

Fig. 9 demonstrates the spatial gradient of P_z/ε_0 along the x-axis. It is also possible that a similar spatial gradient can be created along the y-axis, which is not shown here. Therefore, this spatial tangential gradient in a vector form can be written as $\hat{n} \times \nabla_\parallel (P_n/\varepsilon_0)$ whose unit is [V/m] where $\hat{n}$ is the unit vector normal to the metasurface plane as shown in Fig. 5. The units of the electric surface polarization density and the magnetic surface polarization density are [C/m] and [A], respectively.

Fig. 11 provides a side view of a portion of a sample metasurface illuminated by an incident plane wave at its resonance frequency. This metasurface lies in the xy-plane and is placed between two different material media, region A with ε_A and μ_A and region B with ε_B and μ_B. The figure illustrates how the normal component of the electric surface polarization densities can impact the discontinuity of the tangential electric field across the metasurface.

Fig. 11(a) illustrates that an oblique incident plane wave can excite the normal surface polarization densities of the surface scattering particles (meta-atoms). This happens basically because the normal scattering particles, whose dipole moment vectors are normal to the interface, cannot sense the time-changing fields of a normal incident plane wave. However, by changing the angle of the incident wave, they might be excited [48]. It is important to note that these densities are perfectly spatially uniform, meaning their spatial derivatives along the x-axis are equal to zero. As a result, they do not affect the tangential field discontinuities across the metasurface.

As shown in Fig. 11(c), the electric dipoles are oriented obliquely to the metasurface. Nonetheless, their spatial gradient along the x-axis is also zero, indicating that they do not affect the tangential field discontinuities across the metasurface. In Fig. 11(e), for a general case where the electric dipole moments are randomly placed on the metasurface, they can impact the discontinuity only when the spatial derivative of the normal surface polarization density differs from zero. The purpose of these figures is to demonstrate that P_n is included in the GSTCs if its spatial tangential gradient on the metasurface plane becomes different from zero. Similarly, these figures can be depicted for the normal magnetization density (M_n), whose spatial derivatives (not time derivatives) may cause a discontinuity in the tangential component of the magnetic field across the metasurface. In fact, the gradient of these induced normal electric and magnetic surface polarization vectors can directly influence the discontinuities (or jumps) of the tangential components of electric and magnetic fields across the metasurface. Therefore, they may add or reduce the

amount of field difference on the left-hand side of (9) and (10) [12], [13], [47], [63].

In order to solve the boundary value problems of the metasurface using Maxwell's equations, the tangential spatial derivative component of P_n and M_n on the surface should be considered. This is illustrated in Fig. 11(b), Fig. 11(d), and Fig. 11(e), where Stokes' theorem can be applied to Maxwell's laws. Finally, (9) and (10) can be generalized into the GSTCs, which were derived by Idemen [72] as follows:

$$\hat{n} \times (E_2 - E_1) + \hat{n} \times \nabla_\parallel \left(\frac{P_n}{\varepsilon_0}\right) = -\mu_0 \frac{\partial M_\parallel}{\partial t} \quad (11)$$

$$\hat{n} \times (H_2 - H_1) + \hat{n} \times \nabla_\parallel M_n = J_s + \frac{\partial P_\parallel}{\partial t} \quad (12)$$

where $\nabla_\parallel = \frac{\partial}{\partial t_1}\hat{t}_1 + \frac{\partial}{\partial t_2}\hat{t}_2$.

As shown in Fig. 5, the index of $\hat{t}_1$ and $\hat{t}_2$ are two tangential surface components, so that $\hat{n} = \hat{t}_1 \times \hat{t}_2$. In fact, the surface discontinuity created by the metasurface for electromagnetic fields is more general than the conventional boundary conditions, which assume zero thickness of the metasurface. Regarding the uniqueness theorem, with two main equations of the GSTCs for the discontinuity of the transverse fields across the interface, one can accurately determine the characteristics of any metasurface [9].

Finally, it should be noted that three surface constants have been defined in GSTCs, which will be reviewed in the following sections. These surface constants are used to connect the tangential field discontinuities across the metasurface to the average fields of the metasurface on both sides [58]. Accordingly, several surface approaches have been employed in the GSTCs [6], [58], [67], including the surface (i) susceptibility [9], (ii) polarizability [16], or (iii) electric impedance/magnetic admittance approaches [29], [67], each of them has its own merits. For example, the advantage of the microscopic approach is that we only need the incident plane wave, and the electric (P) and magnetic (μ_0M) surface polarization densities can be related to polarizability tensors [9], [12]. The macroscopic approach, on the other hand, requires the incident, reflection, and transmission fields to calculate the susceptibility tensors [16], [48]. We refer the reader to the relevant literature which covers the theoretical study of these methods extensively [9], [16], [19], [29], [37], [50], [51], [52], [53], [54], [55], [56], [57], [60], [58], [73], [74], [75], [76].

As already mentioned, the primary advantage of the GSTC modeling method lies in its ability to accelerate calculation speeds significantly compared to conventional full-wave simulation methods. While GSTCs serve as a suitable boundary condition for accurately presenting the discontinuities in the tangential fields over metasurfaces, a challenge remains in transforming these GSTCs into a physically meaningful representation. The current study focuses on conceptually understanding GSTCs to characterize a metasurface that effectively showcases the desired EM behavior. Therefore, the next section will investigate how GSTCs can be translated
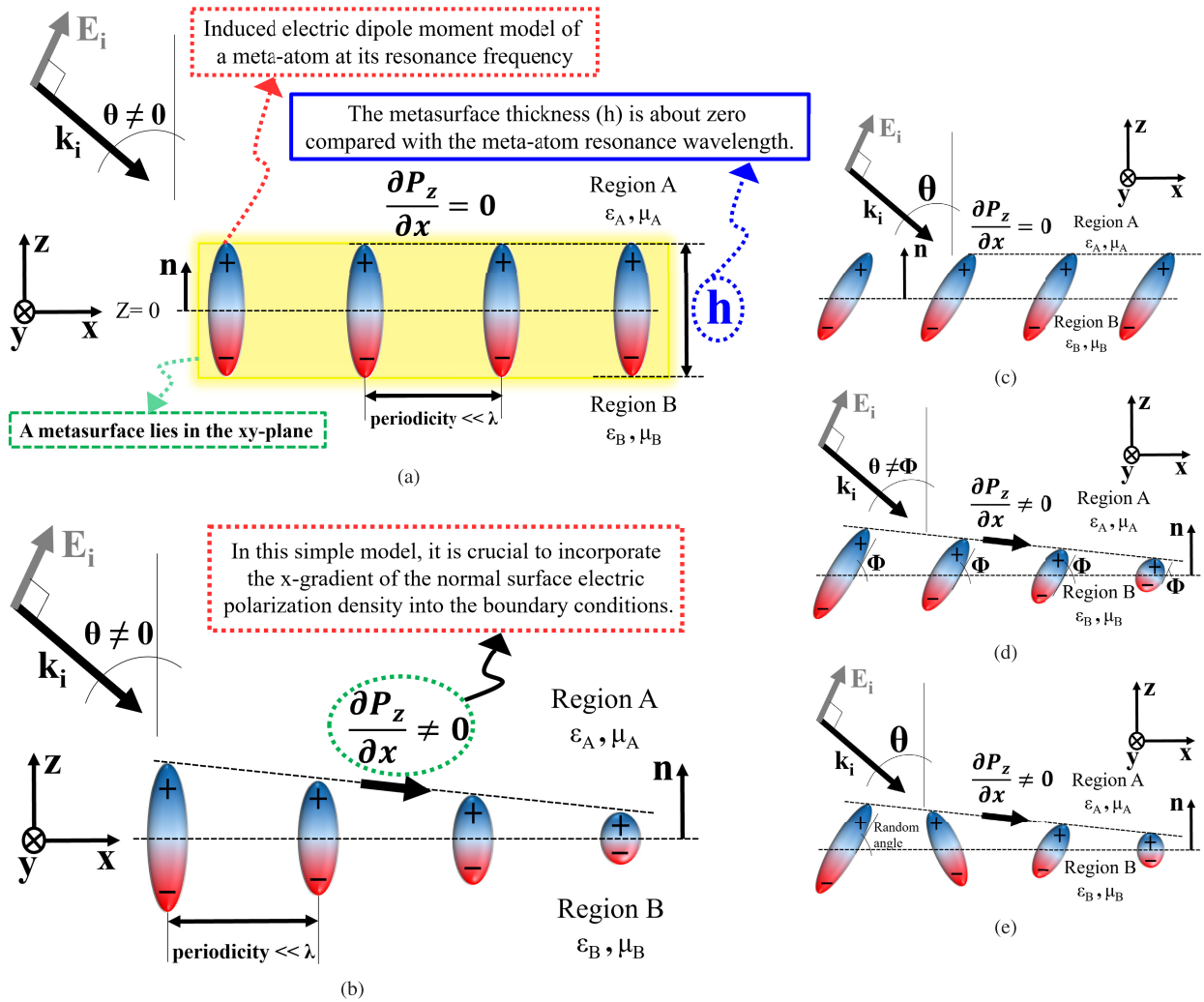
FIGURE 11. A schematic side view of a metasurface sample whose normal electric surface polarization density of electric dipole moments are excited by an incident plane wave. Various orientations of electric dipole moments are shown in the figure, either perpendicular or oblique to the metasurface plane, resulting in (a) $\frac{\partial P_z}{\partial x} = 0$, (b) $\frac{\partial P_z}{\partial x} \neq 0$, (c) $\frac{\partial P_z}{\partial x} = 0$, (d) $\frac{\partial P_z}{\partial x} \neq 0$, and (e) $\frac{\partial P_z}{\partial x} \neq 0$. Only the effect of normal components of these surface polarizations is considered.

into meaningful physical parameters and devise strategies for designing physical structures accordingly.

V. GSTCS MODELING APPROACHES
This section focuses on the challenge of designing scatters and comprehending their properties based on GSTCs, which is essential for controlling and generating the desired electromagnetic field patterns. To address this, one potential approach is to establish a connection between the overall EM fields and the conditions that apply at the metasurface boundaries [8], [19], [67].

A. METASURFACE SYNTHESIS APPROCHES
The process of synthesizing metasurfaces involves determining the metasurface's physical parameters, including its geometrical size and EM properties, to obtain a specific wave transformation [9], [12], [19], [48], [58], [67], and [77]. This synthesis process typically comprises two primary

steps. Firstly, it is essential to establish tensorial quantity functions (e.g., susceptibility or polarizability) in order to customize the metasurface for desired field behaviors. These tensorial functions serve as a library guide for determining the parameters of a metasurface necessary to achieve desired wave characteristics [77]. Secondly, to effectively transform the radiation characteristics of meta-atoms, such as reflection and transmission coefficients, into available libraries based on GSTCs, it is crucial to establish a connection between meta-atom parameters and the tensorial functions [77]. This step involves a full-wave parametric analysis of meta-atoms, considering characteristics such as transmission and reflection coefficients of meta-atoms, amplitude, phase mapping, etc. The goal is to find an optimal arrangement of meta-atom geometry and shape for constructing the desired metasurface under periodic boundary conditions (PBCs) [19], [58], [77]. During this step, full-wave scattering parameters for a unit cell should be computed using 2-D PBCs. This process aims

to identify the scattering particles that can realize the transfer function associated with the synthesized susceptibilities or polarizability or impudence/admittance tensors [48], [58], [77].

Finally, a library containing various subwavelength scattering particles with full-wave characteristics will be generated. This collection greatly assists in establishing a mapping between the properties of these particles and the relationships between susceptibility and incident field. It should be mentioned that the EM response of each subwavelength particle might be expressed through transmission and reflection coefficients. For example, the authors in [74] demonstrate a straightforward design methodology for designing a non-periodic metamaterial Huygens' surfaces. In this work [74], the surface impedances are directly determined from a metasurface's complex transmission (T) and reflection (R) coefficients [78] when a normal incident wave is considered, as follows [74].

$$Y_{es} = \frac{2(1 - T - R)}{\eta(1 + T + R)}, \quad Z_{ms} = \frac{2\eta(1 - T + R)}{(1 + T - R)} \quad (13)$$

where $\eta = \sqrt{\mu_0/\varepsilon_0}$ is the wave impedance of free space.

Hence, a sample-designed meta-atom (e.g., designed cell in Fig. 2 of [74]) can serve as a precise tool for manipulating the tangential components of both transmitted and reflected fields. These calculations are beneficial during interactions with a specified EM incident field. To showcase how GSTCs work, the authors in [74] considered a non-reflecting metasurface to provide an initial relationship that simply connects the transmitted field to the tensorial function and the incident field. Regarding the uniqueness theory, the normal components of the fields are entirely determined by their tangential components [9]. Consequently, the entire generated EM field by the metasurface is realized.

B. SURFACE IMPEDANCE MODEL
In fact, the foundation for these generalized surface boundary conditions is rooted in the connection between magnetic surface current density ($\mathbf{M}_s$) and the average magnetic field ($\mathbf{H}_{t,avg}$), as well as between electric surface current density ($\mathbf{J}_s$) and the average electric field ($\mathbf{E}_{t,avg}$) applied on the metasurface [19]. This connection is established through the utilization of electric surface impedance and magnetic surface admittance, respectively, which are defined in (16) [76]. This signifies that the electric surface current is directly proportional to the average electric field on both sides of the surface [76]. In [19], the author discusses how magnetic surface admittance can be perceived as similar to the concept of magnetic conductance, while electric surface impedance can be conceptually like resistance in Ohm's law. The introduction of these surface constants of proportionality, namely electric impedance and magnetic admittance, leads to the establishment of the two impedance/admittance boundary conditions utilized for describing GSTCs (see Fig. 12) [8],

[16], [19], [65], [67], [74], [76], [79]:

$$\mathbf{E}_{t,avg} = \frac{1}{2}(\mathbf{E}_{1,t} + \mathbf{E}_{2,t}) \quad (14)$$

$$\mathbf{H}_{t,avg} = \frac{1}{2}(\mathbf{H}_{1,t} + \mathbf{H}_{2,t}) \quad (15)$$

$$\mathbf{E}_{t,avg} = \overline{\overline{Z}}_{se}\mathbf{J}_s, \quad \mathbf{H}_{t,avg} = \overline{\overline{Y}}_{sm}\mathbf{M}_s \quad (16)$$

$$\mathbf{E}_{t,avg} = \overline{\overline{Z}}_{se}[\hat{\mathbf{n}} \times (\mathbf{H}_2 - \mathbf{H}_1)] \quad (17)$$

$$\mathbf{H}_{t,avg} = \overline{\overline{Y}}_{sm}[-\hat{\mathbf{n}} \times (\mathbf{E}_2 - \mathbf{E}_1)] \quad (18)$$

Let's assume there is an infinite planar metasurface positioned on the plane of x-y at z = 0, and the unit vector z is normal to its surface. The designed structure is illuminated by an incident plane wave from below, as shown in Fig. 12. The total vectorial fields below and above the metasurface are represented by $\mathbf{E}_1$, $\mathbf{H}_1$ and $\mathbf{E}_2$, $\mathbf{H}_2$ respectively, as shown in Fig. 12. It is important to note that in the equation mentioned above, which links the average fields to the boundary conditions, approximations are introduced in the actual fields that precisely occur within the surface of constitutive components [19], [48], [66], [80]. In addition, two other material proportionality surface constants, surface susceptibility and polarizability, can connect the average fields to the discontinuity of the tangential field on the metasurfaces [19], [58], [65], [67]. Such approximations are also used to represent GSTCs based on the susceptibility and polarizability characteristics [19]. In other words, these three approaches for representing GSTCs require approximated fields, e.g., arithmetic averages of the fields before and after the metasurface, to calculate the tangential field discontinuities across the metasurface [19], [48]. The key rationale for these approximations lies in the challenge of precisely determining the actual field values at the discontinuity boundary [19]. Hence, approximations like the average field are employed due to the difficulties associated with calculating precise values of these fields [19].

C. POLARIZABILITY MODEL
As already mentioned, another simplification in the polarizability modeling of GSTCs formulated by Kuester et al. involves the assumption that conduction currents are negligible in their derivations [16], [19]. The simplification of the GSTCs is beneficial because their derivations involve scatterers that can be magnetized and electrically polarized by magnetic and electric surface polarizabilities. This concept does not involve the conduction currents of free charges [19]. As a result, the relationships of (11) and (12) in the frequency domain are simplified as follows [19]. Note that an $e^{j\omega t}$ time harmonic convention is presumed throughout the paper.

$$\hat{\mathbf{n}} \times (\mathbf{E}_2 - \mathbf{E}_1) + \frac{1}{\varepsilon_0}\hat{\mathbf{n}} \times \nabla_{\parallel}\mathcal{P}_{s,n} = -j\omega\mu_0\boldsymbol{\mathcal{M}}_{s,t} \quad (19)$$

$$\hat{\mathbf{n}} \times (\mathbf{H}_2 - \mathbf{H}_1) + \hat{\mathbf{n}} \times \nabla_{\parallel}\mathcal{M}_{s,n} = j\omega\boldsymbol{\mathcal{P}}_{s,t} \quad (20)$$

where $\mathcal{M}_{s,n}$, $\mathcal{P}_{s,n}$, $\boldsymbol{\mathcal{M}}_{s,t}$ and $\boldsymbol{\mathcal{P}}_{s,t}$ in the frequency domain are the normal surface magnetization density, the normal
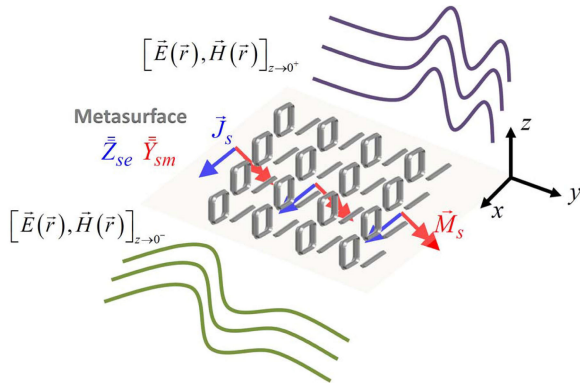
FIGURE 12. Physical arrangement of surface polarizable particles, characterized by the magnetic surface admittance $\overline{\overline{Y}}_{\mathrm{sm}}(x, y)$ and the electric surface impedance $\overline{\overline{Z}}_{\mathrm{se}}(x, y)$ within a general metasurface. The averaged applied field induces the magnetic and electric currents on the metasurface, leading to a discontinuity between the fields above and below the metasurface, resulting in a mechanism to manipulate EM wavefronts Reprinted with permission from [67] ©Optica Publishing Group.

electric surface polarization density, the tangential surface magnetization density and the tangential electric surface polarization density, respectively [19].

The density distributions of surface magnetization and electric surface polarization can generate discontinuities in the macroscopic magnetic and electric fields [16]. However, these densities themselves stem from averaging a distribution comprising discrete magnetic dipole moments ($\boldsymbol{m}$) and electric dipole moments ($\boldsymbol{p}$), which are related to the acting fields as denoted in (21)-(24) [16], [19], [61]. It should be mentioned that dipole moments associated with polarization density can be applied to any media [19]. The study in [16] shows that the magnetization and polarization densities can be represented by effective surface polarizabilities concerning the average fields instead of the acting fields for an infinitesimally thin surface [19]. The magnetic surface polarization density ($\mathcal{M}$) and electric surface polarization density ($\mathcal{P}$) are formulated in (24) based on a microscopic representation of the metasurface responses [16], [19].

$$\mathcal{P} = N \langle \boldsymbol{p} \rangle, \qquad \mathcal{M} = N \langle \boldsymbol{m} \rangle \qquad (21)$$

$$\boldsymbol{p} = \varepsilon_0 \overline{\overline{\alpha}}_{\mathrm{e}} \boldsymbol{E}_{\mathrm{act}}, \qquad \boldsymbol{m} = \overline{\overline{\alpha}}_{\mathrm{m}} \boldsymbol{H}_{\mathrm{act}} \qquad (22)$$

$$\boldsymbol{E}_{\mathrm{act}} = \boldsymbol{E}_{\mathrm{avg}} - \boldsymbol{E}_{\mathrm{scatter}}, \qquad \boldsymbol{H}_{\mathrm{act}} = \boldsymbol{H}_{\mathrm{avg}} - \boldsymbol{H}_{\mathrm{scatter}} \qquad (23)$$

$$\mathcal{P} = \varepsilon_0 N \langle \overline{\overline{\alpha}}_{\mathrm{e}} \rangle \boldsymbol{E}_{\mathrm{act}}, \qquad \mathcal{M} = N \langle \overline{\overline{\alpha}}_{\mathrm{m}} \rangle \boldsymbol{H}_{\mathrm{act}} \qquad (24)$$

In these equations, N represents the count of scatterers per unit area, and the notation < > signifies an averaging process encompassing the scatterers surrounding the points where magnetization and electric surface polarization densities are introduced [9], [16], [19], [61]. In fact, any dipole moment is related to the field that acts upon the scattering particle with the proportionality involving the magnetic and electric surface polarizability tensors of a given scatterer (i.e., $\overline{\overline{\alpha}}_{\mathrm{e}}$ and $\overline{\overline{\alpha}}_{\mathrm{m}}$), as shown in (22) [9], [16]. In the microscopic representation of the metasurface responses

mentioned in (23), the acting (or local) fields' concept involves averaging the fields on either side of the metasurface while considering contributions from all scatters with their coupling effects except the one under consideration [9], [16], [19], [61]. In [16], the contribution of this scatter has been approximately modeled using a very small radius disk containing its magnetic and electric current dipoles [16], [19], [61]. By ''very small'', we refer to a scale where the surface magnetization and electric surface polarization densities are reasonably assumed to remain nearly constant on the disk. In other words, the term ''acting field'' in (23) refers to the local field that is acting on each separate scattering particle, excluding the excited scatterer's own field contribution [16], [19]. In order to characterise the GSTCs based on the surface polarizabilities by combining (19)-(20) with (24), the polarizability boundary conditions are formulated in (25) and (26) and simplified in (27) and (28) [19]. For further details, we direct the reader to [16], [19], and [48].

$$\hat{\boldsymbol{n}} \times (\mathbf{H}_2 - \mathbf{H}_1) = j\omega\varepsilon_0 \left[N \langle \overline{\overline{\alpha}}_{\mathrm{e}} \rangle \boldsymbol{E}_{\mathrm{act}} \right]_{\mathrm{s, t}}$$
$$- \hat{\boldsymbol{n}} \times \nabla_{\|} \left[N \langle \overline{\overline{\alpha}}_{\mathrm{m}} \rangle \boldsymbol{H}_{\mathrm{act}} \right]_{\mathrm{s, n}} \qquad (25)$$

$$-\hat{\boldsymbol{n}} \times (\mathbf{E}_2 - \mathbf{E}_1) = j\omega\mu_0 \left[N \langle \overline{\overline{\alpha}}_{\mathrm{m}} \rangle \boldsymbol{H}_{\mathrm{act}} \right]_{\mathrm{s, t}}$$
$$+ \hat{\boldsymbol{n}} \times \nabla_{\|} \left[N \langle \overline{\overline{\alpha}}_{\mathrm{e}} \rangle \boldsymbol{E}_{\mathrm{act}} \right]_{\mathrm{s, n}} \qquad (26)$$

$$\hat{\boldsymbol{n}} \times (\mathbf{H}_2 - \mathbf{H}_1) = j\omega\varepsilon_0 \overline{\overline{\alpha}}_{\mathrm{E, t}} \boldsymbol{E}_{\mathrm{t,avg}}$$
$$- \hat{\boldsymbol{n}} \times \nabla_{\|} \left[\alpha_{\mathrm{M, n}} \boldsymbol{H}_{\mathrm{n,avg}} \right] \qquad (27)$$

$$-\hat{\boldsymbol{n}} \times (\mathbf{E}_2 - \mathbf{E}_1) = j\omega\mu_0 \overline{\overline{\alpha}}_{\mathrm{M, t}} \boldsymbol{H}_{\mathrm{t,avg}}$$
$$+ \hat{\boldsymbol{n}} \times \nabla_{\|} \left[\alpha_{\mathrm{E, n}} \boldsymbol{E}_{\mathrm{n,avg}} \right] \qquad (28)$$

where t, n and s subscripts are tangential, normal and surface quantities, respectively [19].

D. SUSCEPTIBILTY MODEL
In order to describe the response of the metasurface at a microscopic level, it is essential to properly define the mutual coupling between the neighbouring scattering particles [9], [19]. To avoid the necessity of an intermediary step of the particle polarizability approach involving the connection to acting fields, as shown in (23), a macroscopic representation of polarizability boundary conditions can be derived by substituting the averaged polarizabilities with surface susceptibilities [19]. This means that to macroscopically describe the metasurface, the polarizabilities mentioned earlier are replaced with surface susceptibilities [61]. Kuester et al. in [16] present the fields of the disk as functions of magnetic surface polarization density $\mathcal{M}$ and electric surface polarization density $\mathcal{P}$, enabling the transformation of relations (24) into functions of average fields (29) [19], [61].

$$\mathcal{P} = \varepsilon_0 \overline{\overline{\chi}}_{\mathrm{e}} \boldsymbol{E}_{\mathrm{avg}}, \qquad \mathcal{M} = \overline{\overline{\chi}}_{\mathrm{m}} \boldsymbol{H}_{\mathrm{avg}} \qquad (29)$$

Similarly, equivalent surface susceptibilities have been employed to characterize an infinitesimally thin metasurface, as denoted in (30) and (31) [19]. It should be mentioned that the susceptibility approach can also be generalized for nonlinear (i.e., higher-order susceptibilities) [12], [81], and

time-modulated situations [58].

$$\hat{\boldsymbol{n}} \times (\mathbf{H}_2 - \mathbf{H}_1) = j\omega\varepsilon_0 \overline{\overline{\chi}}_{\mathrm{E,t}} \boldsymbol{E}_{\mathrm{t,avg}}$$
$$- \hat{\boldsymbol{n}} \times \nabla_\parallel [\chi_{\mathrm{M,n}} \boldsymbol{H}_{\mathrm{n,avg}}] \qquad (30)$$

$$-\hat{\boldsymbol{n}} \times (\mathbf{E}_2 - \mathbf{E}_1) = j\omega\mu_0 \overline{\overline{\chi}}_{\mathrm{M,t}} \boldsymbol{H}_{\mathrm{t,avg}}$$
$$+ \hat{\boldsymbol{n}} \times \nabla_\parallel [\chi_{\mathrm{E,n}} \boldsymbol{E}_{\mathrm{n,avg}}] \qquad (31)$$

In fact, these constitutive surface parameters are properties that define how EM fields interact with a surface. While the normal component of surface susceptibilities or polarizabilities can influence the field discontinuities, it can commonly be ignored for designs that do not involve susceptibilities in the normal direction [19], [48]. Thus, susceptibility and polarizability conditions for a mono-anisotropic metasurfaces [53] are reduced, respectively, as follows [19]:

$$\hat{\boldsymbol{n}} \times (\mathbf{H}_2 - \mathbf{H}_1) = j\omega\varepsilon_0 \overline{\overline{\alpha}}_{\mathrm{E,t}} \mathbf{E}_{\mathrm{t,avg}} \qquad (32)$$

$$-\hat{\boldsymbol{n}} \times (\mathbf{E}_2 - \mathbf{E}_1) = j\omega\mu_0 \overline{\overline{\alpha}}_{\mathrm{M,t}} \mathbf{H}_{\mathrm{t,avg}} \qquad (33)$$

and

$$\hat{\boldsymbol{n}} \times (\mathbf{H}_2 - \mathbf{H}_1) = j\omega\varepsilon_0 \overline{\overline{\chi}}_{\mathrm{E,t}} \mathbf{E}_{\mathrm{t,avg}} \qquad (34)$$

$$-\hat{\boldsymbol{n}} \times (\mathbf{E}_2 - \mathbf{E}_1) = j\omega\mu_0 \overline{\overline{\chi}}_{\mathrm{M,t}} \mathbf{H}_{\mathrm{t,avg}} \qquad (35)$$

Neglecting the normal surface magnetization and electric surface polarization densities, these sets of effective constitutive surface parameters can be equivalent, as demonstrated below [19]:

$$\overline{\overline{Y}}_{\mathrm{se}} = \overline{\overline{Z}}_{\mathrm{se}}^{-1} = j\omega\varepsilon_0 \overline{\overline{\alpha}}_{\mathrm{E,t}} \qquad (36)$$

$$\overline{\overline{Z}}_{\mathrm{sm}} = \overline{\overline{Y}}_{\mathrm{sm}}^{-1} = j\omega\mu_0 \overline{\overline{\alpha}}_{\mathrm{M,t}} \qquad (37)$$

and

$$\overline{\overline{Y}}_{\mathrm{se}} = \overline{\overline{Z}}_{\mathrm{se}}^{-1} = j\omega\varepsilon_0 \overline{\overline{\chi}}_{\mathrm{E,t}} \qquad (38)$$

$$\overline{\overline{Z}}_{\mathrm{sm}} = \overline{\overline{Y}}_{\mathrm{sm}}^{-1} = j\omega\mu_0 \overline{\overline{\chi}}_{\mathrm{M,t}} \qquad (39)$$

VI. BIANISOTROPIC BOUNDARY CONDITIONS IN THE DESIGN OF METASURFACES

The descriptions of the GSTCs in the previous section, which include polarizability, susceptibility, and impedance/admittance, exhibit certain limitations. In the previous section, the field discontinuities were just excited by either the acting or averaging magnetic or electric field, but not by both simultaneously [8]. Although GSTCs for mono-anisotropic metasurfaces offer a unique solution for boundary conditions, they might not fully consider the complexities and losses which are in real-world EM interactions [19]. These challenges arise in modeling and understanding EM interactions, particularly at metasurfaces, revealing that some assumptions may not hold in practical scenarios. Therefore, a better approach to enhance the control of boundary conditions is to employ bianisotropy instead of mono-anisotropic metasurface boundary conditions [19], [37], [58], [60], [76], [82].

The bianisotropy approach can potentially alleviate the mentioned issue by introducing magneto-electric and electro-magnetic coupling coefficients to GSTCs, enabling the excitation of magnetic and electric current densities from both magnetic and electric fields. In fact, bianisotropic metasurfaces add an additional degree of freedom to GSTCs in the form of magneto-electric and electro-magnetic coupling tensors of $\overline{\overline{K}}_{\mathrm{me}}$ and $\overline{\overline{K}}_{\mathrm{em}}$, respectively [19], [37], [58], [60], [76], [83]. The use of bianisotropic surface boundaries has the potential to characterize conformal optical and EM systems, which allows them to be incorporated in various platforms. This is due to the fact that the metasurfaces can be characterized by electric, magnetic, and magneto-electric/electro-magnetic responses [12], [19], [61], [84], [85], [86]. Therefore, the GSTCs in (16) can be reformulated for the bianisotropic metasurfaces in a manner involving surface impedances, admittances, electro-magnetic coupling and magneto-electric coupling coefficients as follows [8], [19].

$$\boldsymbol{E}_{\mathrm{t,avg}} = \overline{\overline{Z}}_{\mathrm{se}} \boldsymbol{J}_{\mathrm{s}} - \overline{\overline{K}}_{\mathrm{em}} [\hat{\boldsymbol{n}} \times \boldsymbol{M}_{\mathrm{s}}] \qquad (40)$$

$$\boldsymbol{H}_{\mathrm{t,avg}} = \overline{\overline{Y}}_{\mathrm{sm}} \boldsymbol{M}_{\mathrm{s}} + \overline{\overline{K}}_{\mathrm{me}} [\hat{\boldsymbol{n}} \times \boldsymbol{J}_{\mathrm{s}}] \qquad (41)$$

In order to better understand similarities among various modeling approaches of GSTCs, such as the surface impedance boundary conditions and other constituent surface parameters, we also provide a brief overview of bianisotropic polarizability and susceptibility boundary conditions. For more details, the reader is referred to [9], [12], [19], [48], [58], and [84]. It should be noted that designing metasurfaces with bianisotropic boundary conditions needs scattering particles exhibiting magneto-electric/electro-magnetic properties. The most recent review paper [58] on bianisotropic metasurfaces demonstrates that complex magnetic, electric, magneto-electric and electro-magnetic susceptibilities, incorporating gain and loss, can enable arbitrary field transformations using bianisotropic boundaries.

In the following, we will review this by considering the interaction of both the acting and averaging electric and magnetic fields in generating surface magnetization and electric surface polarization densities [9], [19], [61].

$$\mathcal{P} = \varepsilon_0 N \langle \overline{\overline{\alpha}}_{\mathrm{ee}} \rangle \boldsymbol{E}_{\mathrm{act}} + \sqrt{\mu_0 \varepsilon_0} N \langle \overline{\overline{\alpha}}_{\mathrm{em}} \rangle \boldsymbol{H}_{\mathrm{act}} \qquad (42)$$

$$\mathcal{M} = N \langle \overline{\overline{\alpha}}_{\mathrm{mm}} \rangle \boldsymbol{H}_{\mathrm{act}} + \sqrt{\frac{\varepsilon_0}{\mu_0}} N \langle \overline{\overline{\alpha}}_{\mathrm{me}} \rangle \boldsymbol{E}_{\mathrm{act}} \qquad (43)$$

By substituting the bianisotropic parameters from (42) and (43) with those in (19) and (20), the bianisotropic polarizability modeling of GSTCs can be obtained, as denoted in follows [19], [58].

$$\hat{\boldsymbol{n}} \times (\mathbf{H}_2 - \mathbf{H}_1) = j\omega \big[\varepsilon_0 N \langle \overline{\overline{\alpha}}_{\mathrm{ee}} \rangle \boldsymbol{E}_{\mathrm{act}}$$
$$+ \sqrt{\mu_0 \varepsilon_0} N \langle \overline{\overline{\alpha}}_{\mathrm{em}} \rangle \boldsymbol{H}_{\mathrm{act}} \big]_{\mathrm{s,t}}$$
$$- \hat{\boldsymbol{n}} \times \nabla_\parallel \big[N \langle \overline{\overline{\alpha}}_{\mathrm{mm}} \rangle \boldsymbol{H}_{\mathrm{act}}$$
$$+ \sqrt{\frac{\varepsilon_0}{\mu_0}} N \langle \overline{\overline{\alpha}}_{\mathrm{me}} \rangle \boldsymbol{E}_{\mathrm{act}} \big]_{\mathrm{s,n}} \qquad (44)$$

$$-\hat{\boldsymbol{n}} \times (\mathbf{E}_2 - \mathbf{E}_1) = j\omega\mu_0 \left[N \langle \overline{\overline{\alpha}}_{\text{mm}} \rangle \boldsymbol{H}_{\text{act}} \right.$$
$$+ \sqrt{\frac{\varepsilon_0}{\mu_0}} N \langle \overline{\overline{\alpha}}_{\text{me}} \rangle \boldsymbol{E}_{\text{act}} \bigg]_{\text{s,t}}$$
$$+ \frac{1}{\varepsilon_0} \hat{\boldsymbol{n}} \times \nabla_\parallel \left[\varepsilon_0 N \langle \overline{\overline{\alpha}}_{\text{ee}} \rangle \boldsymbol{E}_{\text{act}} \right.$$
$$+ \sqrt{\mu_0\varepsilon_0} N \langle \overline{\overline{\alpha}}_{\text{em}} \rangle \boldsymbol{H}_{\text{act}} \bigg]_{\text{s,n}} \quad (45)$$

In addition, a similar mathematical approach is developed to the bianisotropic susceptibility modeling of GSTCs outlined in follows [19], [58].

$$\mathcal{P} = \varepsilon_0 \overline{\overline{\chi}}_{\text{ee}} \boldsymbol{E}_{\text{avg}} + \sqrt{\mu_0\varepsilon_0} \overline{\overline{\chi}}_{\text{em}} \boldsymbol{H}_{\text{avg}} \quad (46)$$

$$\mathcal{M} = \overline{\overline{\chi}}_{\text{mm}} \boldsymbol{H}_{\text{avg}} + \sqrt{\frac{\varepsilon_0}{\mu_0}} \overline{\overline{\chi}}_{\text{me}} \boldsymbol{E}_{\text{avg}} \quad (47)$$

$$\hat{\boldsymbol{n}} \times (\mathbf{H}_2 - \mathbf{H}_1) = j\omega \left[\varepsilon_0 \overline{\overline{\chi}}_{\text{ee}} \mathbf{E}_{\text{avg}} + \sqrt{\mu_0\varepsilon_0} \overline{\overline{\chi}}_{\text{em}} \mathbf{H}_{\text{avg}} \right]_{\text{s,t}}$$
$$- \hat{\boldsymbol{n}} \times \nabla_\parallel \left[\overline{\overline{\chi}}_{\text{mm}} \mathbf{H}_{\text{avg}} + \sqrt{\frac{\varepsilon_0}{\mu_0}} \overline{\overline{\chi}}_{\text{me}} \mathbf{E}_{\text{avg}} \right]_{\text{s,n}}$$
$$(48)$$

$$-\hat{\boldsymbol{n}} \times (\mathbf{E}_2 - \mathbf{E}_1) = j\omega\mu_0 \left[\overline{\overline{\chi}}_{\text{mm}} \mathbf{H}_{\text{avg}} + \sqrt{\frac{\varepsilon_0}{\mu_0}} \overline{\overline{\chi}}_{\text{me}} \mathbf{E}_{\text{avg}} \right]_{\text{s,t}}$$
$$+ \frac{1}{\varepsilon_0} \hat{\boldsymbol{n}} \times \nabla_\parallel \left[\varepsilon_0 \overline{\overline{\chi}}_{\text{ee}} \mathbf{E}_{\text{avg}} \right.$$
$$+ \sqrt{\varepsilon_0\mu_0} \overline{\overline{\chi}}_{\text{em}} \mathbf{H}_{\text{avg}} \bigg]_{\text{s,n}} \quad (49)$$

The surface susceptibility tensors in (46) and (47) consist of the magnetic $\overline{\overline{\chi}}_{\text{mm}}$, the electric $\overline{\overline{\chi}}_{\text{ee}}$, the magneto-electric $\overline{\overline{\chi}}_{\text{me}}$ and the electro-magnetic $\overline{\overline{\chi}}_{\text{em}}$ tensors [58]. Each of the tensors can have a 3×3 dimension. Additionally, the most general bianisotropic metasurface structure can be characterized by 36 general susceptibility or polarizability parameters [61], [84]. For instance, the magnetic susceptibility tensor in a Cartesian coordinate system is [58]:

$$\overline{\overline{\chi}}_{\text{mm}} = \begin{bmatrix} \chi_{\text{mm}}^{xx} & \chi_{\text{mm}}^{xy} & \chi_{\text{mm}}^{xz} \\ \chi_{\text{mm}}^{yx} & \chi_{\text{mm}}^{yy} & \chi_{\text{mm}}^{yz} \\ \chi_{\text{mm}}^{zx} & \chi_{\text{mm}}^{zy} & \chi_{\text{mm}}^{zz} \end{bmatrix} \quad (50)$$

However, it is worth noting that in some cases, it is convenient to assume that the metasurface has zero normal polarizability or susceptibility components; the number of tangential susceptibilities can be reduced to 16, as shown in (52) [48], [84]. Therefore, (48) and (49) can be written as (51).

$$\begin{bmatrix} \Delta\mathbf{H}_y \\ \Delta\mathbf{H}_x \\ \Delta\mathbf{E}_y \\ \Delta\mathbf{E}_x \end{bmatrix} = \begin{bmatrix} \tilde{\chi}_{\text{ee}}^{xx} & \tilde{\chi}_{\text{ee}}^{xy} & \tilde{\chi}_{\text{em}}^{xx} & \tilde{\chi}_{\text{em}}^{xy} \\ \tilde{\chi}_{\text{ee}}^{yx} & \tilde{\chi}_{\text{ee}}^{yy} & \tilde{\chi}_{\text{em}}^{yx} & \tilde{\chi}_{\text{em}}^{yy} \\ \tilde{\chi}_{\text{me}}^{xx} & \tilde{\chi}_{\text{me}}^{xy} & \tilde{\chi}_{\text{mm}}^{xx} & \tilde{\chi}_{\text{mm}}^{xy} \\ \tilde{\chi}_{\text{me}}^{yx} & \tilde{\chi}_{\text{me}}^{yy} & \tilde{\chi}_{\text{mm}}^{yx} & \tilde{\chi}_{\text{mm}}^{yy} \end{bmatrix} \begin{bmatrix} \mathbf{E}_{x,\text{av}} \\ \mathbf{E}_{y,\text{av}} \\ \mathbf{H}_{x,\text{av}} \\ \mathbf{H}_{y,\text{av}} \end{bmatrix} \quad (51)$$

In (51) and (52), the tilde symbol $\sim$ is used to represent normalized susceptibilities, which exhibit a connection with the susceptibilities that have not been normalized, as described by (52) [48].

$$\begin{bmatrix} \chi_{\text{ee}}^{xx} & \chi_{\text{ee}}^{xy} & \chi_{\text{em}}^{xx} & \chi_{\text{em}}^{xy} \\ \chi_{\text{ee}}^{yx} & \chi_{\text{ee}}^{yy} & \chi_{\text{em}}^{yx} & \chi_{\text{em}}^{yy} \\ \chi_{\text{me}}^{xx} & \chi_{\text{me}}^{xy} & \chi_{\text{mm}}^{xx} & \chi_{\text{mm}}^{xy} \\ \chi_{\text{me}}^{yx} & \chi_{\text{me}}^{yy} & \chi_{\text{mm}}^{yx} & \chi_{\text{mm}}^{yy} \end{bmatrix}$$

$$= \begin{bmatrix} \frac{j}{\omega\varepsilon_0}\tilde{\chi}_{\text{ee}}^{xx} & \frac{j}{\omega\varepsilon_0}\tilde{\chi}_{\text{ee}}^{xy} & \frac{j}{k_0}\tilde{\chi}_{\text{em}}^{xx} & \frac{j}{k_0}\tilde{\chi}_{\text{em}}^{xy} \\ \frac{-j}{\omega\varepsilon_0}\tilde{\chi}_{\text{ee}}^{yx} & \frac{-j}{\omega\varepsilon_0}\tilde{\chi}_{\text{ee}}^{yy} & \frac{-j}{k_0}\tilde{\chi}_{\text{em}}^{yx} & \frac{-j}{k_0}\tilde{\chi}_{\text{em}}^{yy} \\ \frac{-j}{k_0}\tilde{\chi}_{\text{me}}^{xx} & \frac{-j}{k_0}\tilde{\chi}_{\text{me}}^{xy} & \frac{-j}{\omega\mu_0}\tilde{\chi}_{\text{mm}}^{xx} & \frac{-j}{\omega\mu_0}\tilde{\chi}_{\text{mm}}^{xy} \\ \frac{j}{k_0}\tilde{\chi}_{\text{me}}^{yx} & \frac{j}{k_0}\tilde{\chi}_{\text{me}}^{yy} & \frac{j}{\omega\mu_0}\tilde{\chi}_{\text{mm}}^{yx} & \frac{j}{\omega\mu_0}\tilde{\chi}_{\text{mm}}^{yy} \end{bmatrix} \quad (52)$$

The array equation specified in (52) involves 16 unknown variables, which results in a heavily underdetermined system that is not well-constrained when combined with the matrix equivalents of (51) [48]. In order to solve the inverse synthesis problem presented in (51), there are three primary approaches discussed in [48]. (I) Variable reduction method: This aims to reduce the 16 unknown variables to four, making system (51) solvable or determinate. Several sets of four susceptibility parameters can be assumed as valid candidates for solving the matrix equations of (52), meaning that different combinations of variables can generate the same scattered EM fields. (II) Transformation increase method: Instead of decreasing the number of susceptibility variables to four, this approach focuses on increasing the number of transformations. In other words, the metasurface can be designed to transform multiple sets of transmitted, reflected and incident waves simultaneously. (III) Combination Approach: This method combines the abovementioned techniques to find an effective solution. Various strategies for transforming equation (52) into determinate forms are explained in detail in [48].

In the next section, we will present some typical examples. These examples demonstrate the verification of analytically synthesized approaches (polarizability, susceptibility, and impedance/admittance) often utilized to design various metasurface devices.

VII. EXAMPLES OF DESIGNED METASURFACES
In this section, we indicate some examples of designed metasurfaces to show the validation of the GSTCs method for designing metasurface structures.

A. SYNTHESIZING A HUYGEN'S METASURFACE WITH IMPEDANCE AND ADMITTANCE MODELING OF GSTCS
One advantage of GSTCs is their capability to characterize nonperiodic subwavelength structures that demonstrate responses to both magnetic and electric fields, similar to Huygens metasurfaces [19]. In fact, Huygens' principle states that every individual point found on a wavefront operates as a fictitious secondary source, generating the outgoing wavefront [74]. In 1901, Love extended Huygens' principle rigorously, determining secondary sources as virtual magnetic and electric current densities [19], [74]. Then, Schelkunoff further developed the equivalence principle of Love to encompass any arbitrary EM field distributions on either side of a sheet [74]. The equivalence principle clarifies how any EM wave can be represented using a collection of current densities and any other wave [19]. In [74], the authors presented a simple design method for tailoring wave fronts based on a non-periodic reflectionless Huygens surface. We will review this method further below.
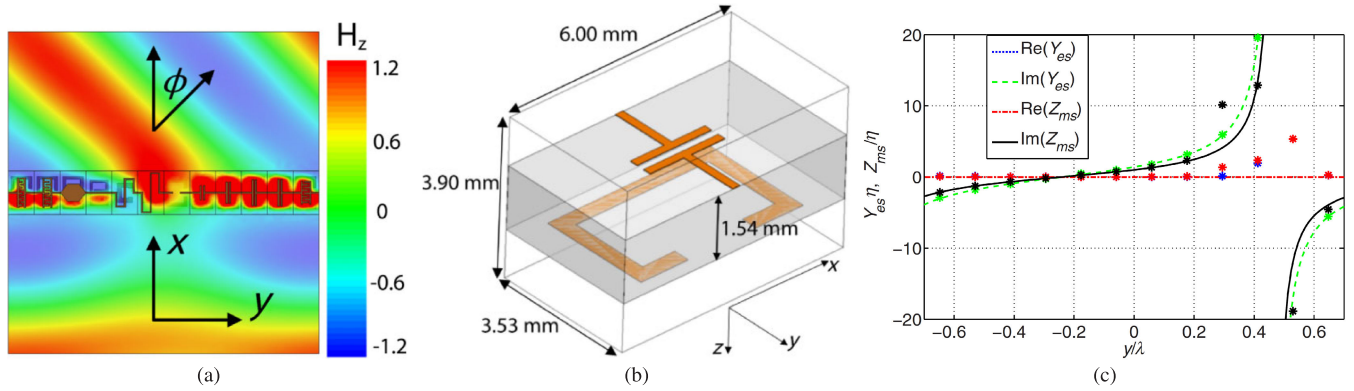
FIGURE 13. (a) A snapshot of the magnetic field simulation result while the designed metasurface is illuminated by a normal incident plane wave, (b) one of the designed metasurface cell configurations which have $Y_{es} = (0.02 + 3.14j)/\eta$ and $Z_{ms} = (0.07 + 2.3j)\eta$, (c) a single period depicting the imaginary and real surface admittances and impedances, computed for refracting a plane wave incident at a normal angle to an oblique angle of 45°. Reprinted figures with permission from [74] Copyright (2013) by the American Physical Society.

Generally, surface impedance and admittance are tensorial quantities. In this particular example [74], they assumed the surface impedance and admittance are isotropic for a surface situated at x = 0, as denoted below (see Fig. 13).

$$Y_{es} = Y_{es}^{yy} = Y_{es}^{zz} \tag{53}$$

$$Z_{ms} = Z_{ms}^{yy} = Z_{ms}^{zz} \tag{54}$$

As already mentioned, these electric surface admittance and magnetic surface impedance can be calculated by using (13) [74]. As depicted in Fig. 13(a), this Huygens' metasurface was engineered to redirect a plane wave, transforming a normal incident wave in Region I to a ϕ = 45° angle in Region II, which is a 45° difference from the normal direction. Fig. 13(a) shows a snapshot of the magnetic field simulation results before and after the plane wave incident on the designed metasurface in Regions I and II, respectively [74]. Therefore, the fields within Regions I and II are as follows [74].

$$\mathbf{E}_1 = -\hat{\mathbf{y}}e^{-jkx} \tag{55}$$

$$\mathbf{H}_1 = -\frac{\hat{\mathbf{z}}}{\eta}e^{-jkx} \tag{56}$$

$$\mathbf{E}_2 = 2^{1/4}(\hat{\mathbf{x}}\sin(\phi) - \hat{\mathbf{y}}\cos(\phi))e^{-jk(y\sin(\phi)+x\cos(\phi))} \tag{57}$$

$$\mathbf{H}_2 = -\hat{\mathbf{z}}\frac{2^{1/4}}{\eta}e^{-jk(y\sin(\phi)+x\cos(\phi))} \tag{58}$$

The resulting electric surface admittance and magnetic surface impedance are calculated according to (59) and (60) [74], respectively.

$$Y_{es} = \frac{2\left(H_1^z - H_2^z\right)}{E_1^y + E_2^y} = \frac{2 - 2^{5/4}e^{-jky\sin(\phi)}}{\eta + 2^{1/4}\eta\cos(\phi)e^{-jky\sin(\phi)}} \tag{59}$$

$$Z_{ms} = \frac{2\left(E_1^y - E_2^y\right)}{H_1^z + H_2^z} = \frac{2\eta - 2^{5/4}\eta\cos(\phi)e^{-jky\sin(\phi)}}{1 + 2^{1/4}e^{-jky\sin(\phi)}} \tag{60}$$

It should be noted that the transmitted and incident waves are plane waves. The surface impedances in the y-axis direction are periodic with a period length equal
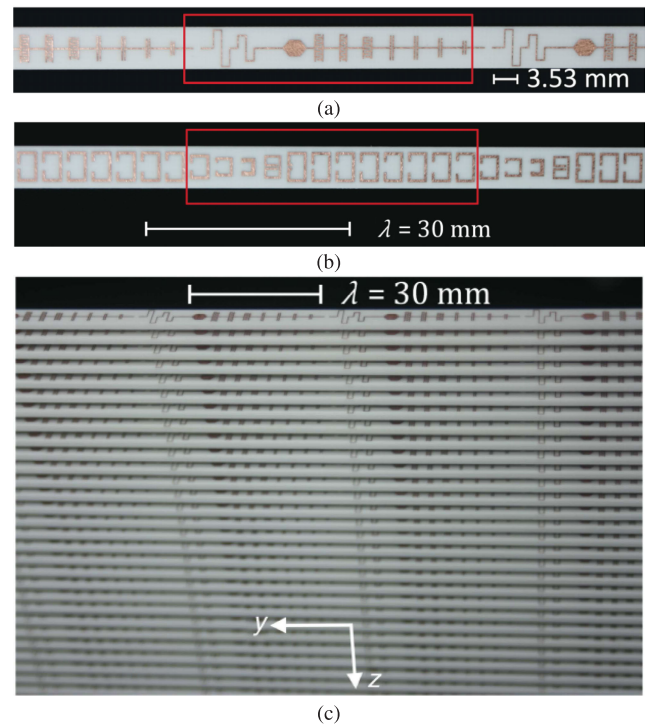
FIGURE 14. A schematic view of the metallic patterns on both the (a) bottom and (b) top layers of the designed metasurface substrate, and (c) a picture of the manufactured metasurface, designed to refract a normal incident plane wave to an oblique angle of 45° at 10 Ghz. Reprinted figures with permission from [74] Copyright (2013) by the American Physical Society.

to $\lambda = \sin(\phi)$ [74]. In order to design this Huygens' metasurface with magnetic surface impedance and electric surface admittance, each period is divided into 12 individual unit cells [74], which consist of designed copper pathways over a Rogers 4003 substrate. To realize each type of electric surface reactance, the upper layer of the substrate is loaded with copper traces in both inductive and capacitive configurations. On the other hand, the lower layer of the designed cell is loaded with capacitive loop resonators to

create magnetic surface reactance. As an example, one of the 12 cells with an electric surface admittance value of $Y_{es} = (0.02 + 3.14j)/\eta$ and a magnetic surface admittance value of $Z_{ms} = (0.07 + 2.3j)\eta$ is illustrated in Fig. 13(b). Where η is the wave impedance of free space. In addition, the normalized magnetic surface impedance and electric surface admittance of a period of 12 cells are shown in Fig. 13(c). Subsequently, a reflectionless Huygens surface is designed using the HFSS full-wave simulator, and their simulation results are compared with the analytical calculation results in [74]. A more in-depth discussion of this example can also be found in [74]. Finally, the ultimate structure based on the Rogers 4003 substrate was designed and implemented, as shown in Fig. 14.

B. SYNTHESIZING A TWIST POLARIZER WITH POLARIZABILITY MODELING OF GSTCS

In the field of bianisotropic metasurface arrays, the theory of EM interactions among electrically small magneto-electric/electro-magnetic scattering particles in a planar square array, with the lattice (grid) periodicity of α constant, is well-known [65], [87], [88], [89]. In order to provide the required polarizabilities of meta-atoms that constitute the metasurface with the desired functionality, an analytical method has been developed in [34], [87], and [88]. In this method, effective polarizabilities are introduced which are denoted with hatted symbols such as $\overline{\overline{\widehat{\alpha}}}_{ee}$, $\overline{\overline{\widehat{\alpha}}}_{mm}$, $\overline{\overline{\widehat{\alpha}}}_{em}$, $\overline{\overline{\widehat{\alpha}}}_{me}$ to simplify the linear relations between the induced dipole moments (**p** and **m**) and the local field at the location of electrically small particles [34], [88]. These effective polarizabilities are the functions relying on interaction dyadics, defined in [65], and particle polarizabilities. By employing these effective polarizabilities, it is possible to establish a linear relationship between the incident EM wave and the induced dipole moment, which is described in (61) [34], [87]. This method facilitates the synthesis of bianisotropic metasurfaces featuring specific transmission and reflection by assuming a plane wave incidence as follows. The form of time harmonic dependence is also $e^{j\omega t}$ [87].

$$\begin{bmatrix} \mathbf{p} \\ \mathbf{m} \end{bmatrix} = \begin{bmatrix} \overline{\overline{\widehat{\alpha}}}_{ee} & \overline{\overline{\widehat{\alpha}}}_{em} \\ \overline{\overline{\widehat{\alpha}}}_{me} & \overline{\overline{\widehat{\alpha}}}_{mm} \end{bmatrix} \cdot \begin{bmatrix} \mathbf{E}_{inc} \\ \mathbf{H}_{inc} \end{bmatrix} \quad (61)$$

$$\mathbf{E}_r = -\frac{j\omega}{2S}\left[\left(\eta_0\widehat{\alpha}_{ee}^{xx} - \widehat{\alpha}_{em}^{xy} + \widehat{\alpha}_{me}^{xy} - \frac{1}{\eta_0}\widehat{\alpha}_{mm}^{yy} \right) \mathbf{\hat{x}\hat{x}} \right.$$
$$+ \left(\eta_0\widehat{\alpha}_{ee}^{xy} + \widehat{\alpha}_{em}^{xx} + \widehat{\alpha}_{me}^{yy} + \frac{1}{\eta_0}\widehat{\alpha}_{mm}^{yx} \right) \mathbf{\hat{x}\hat{y}}$$
$$+ \left(\eta_0\widehat{\alpha}_{ee}^{yx} - \widehat{\alpha}_{em}^{yy} - \widehat{\alpha}_{me}^{xx} + \frac{1}{\eta_0}\widehat{\alpha}_{mm}^{xy} \right) \mathbf{\hat{y}\hat{x}}$$
$$+ \left. \left(\eta_0\widehat{\alpha}_{ee}^{yy} + \widehat{\alpha}_{em}^{yx} - \widehat{\alpha}_{me}^{xy} - \frac{1}{\eta_0}\widehat{\alpha}_{mm}^{xx} \right) \mathbf{\hat{y}\hat{y}} \right] \cdot \mathbf{E}_{inc}$$
$$(62)$$

$$\mathbf{E}_t = \left\{ \left[1 - \frac{j\omega}{2S}\left(\eta_0\widehat{\alpha}_{ee}^{xx} - \widehat{\alpha}_{em}^{xy} - \widehat{\alpha}_{me}^{yx} + \frac{1}{\eta_0}\widehat{\alpha}_{mm}^{yy} \right) \right] \mathbf{\hat{x}\hat{x}} \right.$$

$$+ \left[1 - \frac{j\omega}{2S}\left(\eta_0\widehat{\alpha}_{ee}^{yy} + \widehat{\alpha}_{em}^{yx} + \widehat{\alpha}_{me}^{xy} + \frac{1}{\eta_0}\widehat{\alpha}_{mm}^{xx} \right) \right] \mathbf{\hat{y}\hat{y}}$$
$$- \frac{j\omega}{2S}\left(\eta_0\widehat{\alpha}_{ee}^{yx} - \widehat{\alpha}_{em}^{yy} + \widehat{\alpha}_{me}^{xx} - \frac{1}{\eta_0}\widehat{\alpha}_{mm}^{xy} \right) \mathbf{\hat{y}\hat{x}}$$
$$- \left. \frac{j\omega}{2S}\left(\eta_0\widehat{\alpha}_{ee}^{xy} + \widehat{\alpha}_{em}^{xx} - \widehat{\alpha}_{me}^{yy} - \frac{1}{\eta_0}\widehat{\alpha}_{mm}^{yx} \right) \mathbf{\hat{x}\hat{y}} \right\} \cdot \mathbf{E}_{inc}$$
$$(63)$$

where η_0 is the free space impedance, and S is the unit-cell area [88]. In this example [87], the authors synthesized a twist polarizer illuminated by a linearly polarized incident plane wave. This metasurface polarizer can rotate the transmitted wave's polarisation by 90° without any reflection [34], [87]. As a result, by knowing the incident, transmitted, and reflected waves, we can express them using the following mathematical relationships, which are discussed in detail in [34] and [87].

$$\mathbf{E}_{inc} = E_0\mathbf{\hat{x}} \Rightarrow \begin{cases} \mathbf{E}_r = 0 \\ \mathbf{E}_t = -AE_0\mathbf{\hat{y}} \end{cases} \quad (64)$$

$$\mathbf{E}_{inc} = E_0\mathbf{\hat{y}} \Rightarrow \begin{cases} \mathbf{E}_r = 0 \\ \mathbf{E}_t = AE_0\mathbf{\hat{x}} \end{cases} \quad (65)$$

where A is any complex number (|A| = 1), thus allowing the selection of any phase for the transmitted wave [88]. The effective polarizabilities can be simply found by substituting (64) and (65) into (62) and (63). As already mentioned, there is also a simplification in this example, considering only yy and xx-directed terms in the dyadics of effective polarizability. Therefore, the effective polarizability of this example can be described as follows [87].

$$\eta_0^2\widehat{\alpha}_{ee}^{xx} = \widehat{\alpha}_{mm}^{yy} \quad (66)$$

$$\widehat{\alpha}_{me}^{xy} = -\widehat{\alpha}_{em}^{yy} \quad (67)$$

$$-\widehat{\alpha}_{em}^{yy} + \widehat{\alpha}_{me}^{xx} = 2\widehat{\alpha}_{me}^{xx} = \frac{2S}{j\omega}A \quad (68)$$

And similarly, (65) can be simplified as follows [87].

$$\eta_0^2\widehat{\alpha}_{ee}^{yy} = \widehat{\alpha}_{mm}^{xx} \quad (69)$$

$$\widehat{\alpha}_{em}^{xx} = -\widehat{\alpha}_{me}^{yy} \quad (70)$$

$$\widehat{\alpha}_{em}^{xx} - \widehat{\alpha}_{me}^{yy} = 2\widehat{\alpha}_{em}^{xx} = -\frac{2S}{j\omega}A \quad (71)$$

The process of designing a metasurface starts by defining its functionality and choosing a unit cell from a library that can provide the desired electromagnetic responses. Next, assumptions are made about how the metasurface will respond to electromagnetic waves. This leads to obtaining simplified susceptibility values, followed by establishing a connection between the equations derived from GSTCs and the responses of the unit cells, taking into account the desired geometry and dimensions. Therefore, it is crucial to have a comprehensive understanding of how different basic unit cells respond to electromagnetic waves, their geometries, and their polarizability relationships to design efficient metasurfaces based on GSTCs.
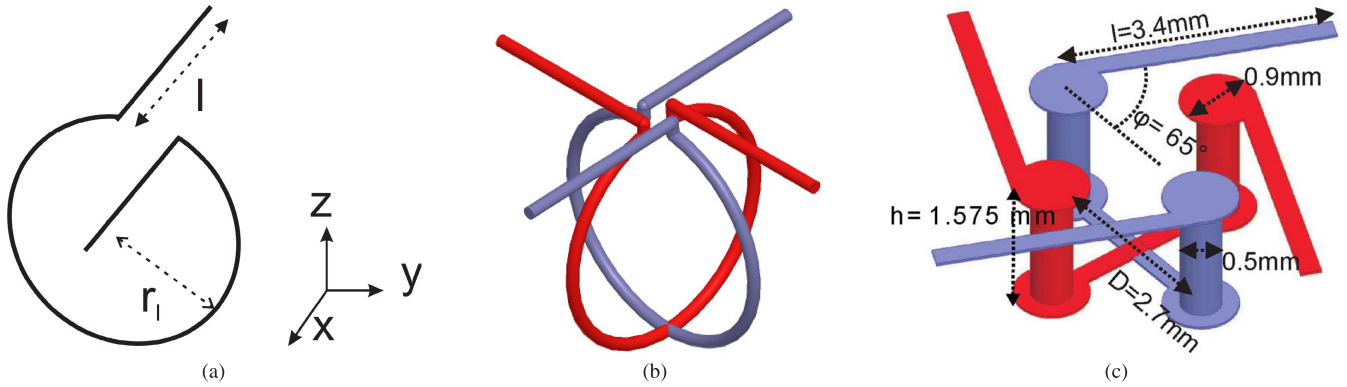
FIGURE 15. A schematic view of (a) a single chiral element [87], (b) a twist polarizer composed of two perpendicular chiral particles [87], and (c) a practical printed circuit board (PCB) implementation of a twist polarizer [34].

For instance, this example [87] exhibits a high degree of symmetry, where the yy components are equal to the xx components. By setting the value of $A = j$, the performance of these effective polarizabilities becomes similar to the canonical helical polarizabilities [87]. Thus, chiral cells (pairs of orthogonal canonical helices) are identified to obtain the well-known geometry, as shown in Fig. 15.

To implement the designed structure based on GSTCs, the authors in [34] and [87] modified the chiral meta-atoms on a PCB, as depicted in Fig. 15(c). Therefore, the individual polarizabilities of a canonical helix can be expressed in terms of wire length l and the loop radius r_1 as follows [34], [87].

$$\alpha_{ee} = \frac{l^2}{j\omega(Z_l + Z_w)} \tag{72}$$

$$\alpha_{em} = -\alpha_{me} = -\mu_0 \frac{\pi r_1^2 l}{Z_l + Z_w} \tag{73}$$

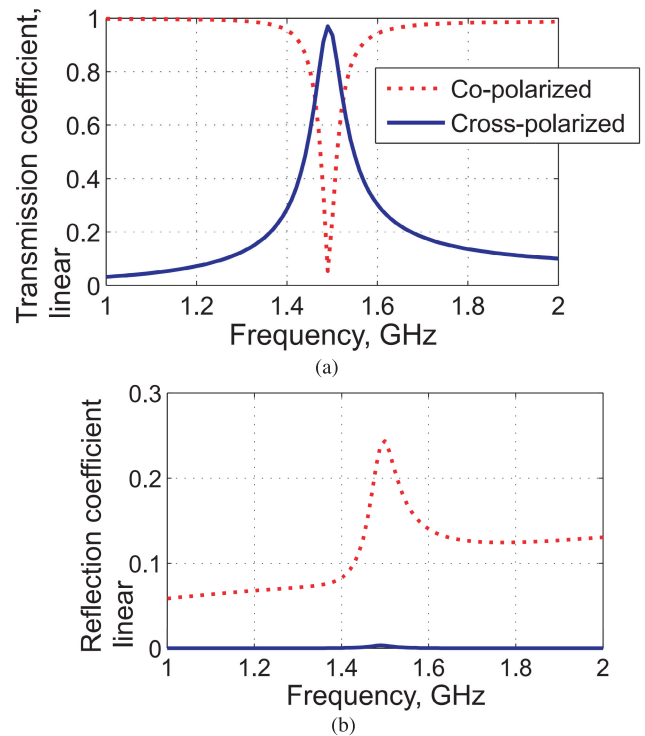$$\alpha_{mm} = -\mu_0^2 \frac{j\omega(\pi r_1^2)^2}{Z_l + Z_w} \tag{74}$$

Basically, the impedance of the particle at resonance frequency is a pure real value. Therefore, the particle impedance can be approximated by the total radiative resistance at its resonance frequency as follows [34].

$$Z_l + Z_w = \frac{\eta_0}{6\pi}\left(k_0^2 l^2 + k_0^4 \left(\pi r_1^2\right)^2\right) \tag{75}$$

Finally, the polarizability equations can also be easily rewritten as denoted by effective polarizability in (76) and (77).

$$\widehat{\alpha}_{ee} = \frac{\alpha_{ee}}{1 - \beta_{ee}\left(\alpha_{ee} + \frac{\alpha_{mm}}{\eta_0^2}\right)} = \frac{\alpha^2}{j\omega\eta_0} \tag{76}$$

$$\widehat{\alpha}_{em} = \frac{\alpha_{em}}{1 - \beta_{ee}\left(\alpha_{ee} + \frac{\alpha_{mm}}{\eta_0^2}\right)} = -\frac{\alpha^2}{\omega} \tag{77}$$

FIGURE 16. The simulation results of the (a) transmitted and (b) reflected fields for both co- and cross-polarized components [87].

$$\widehat{\alpha}_{mm} = \eta_0^2 \widehat{\alpha}_{ee} \tag{78}$$

Assuming a frequency of $f_0 = 1.5$ GHz and considering the unit cell area as $S = a^2 = (40\,\text{mm})^2 = (\lambda_0/5)^2$, the analytically calculated cell dimensions are optimally determined in [87] as $r_1 = 11.7$ mm and $l = 13.5$ mm. This example has been implemented and validated through numerical full-wave simulation using HFSS, as derived by Niemi et al. [34], [87]. Some of their results are shown in Fig. 16. Their simulation results are also compared with the values obtained from metasurface synthesis [34], [87]. It is worth mentioning that the simplifications made during
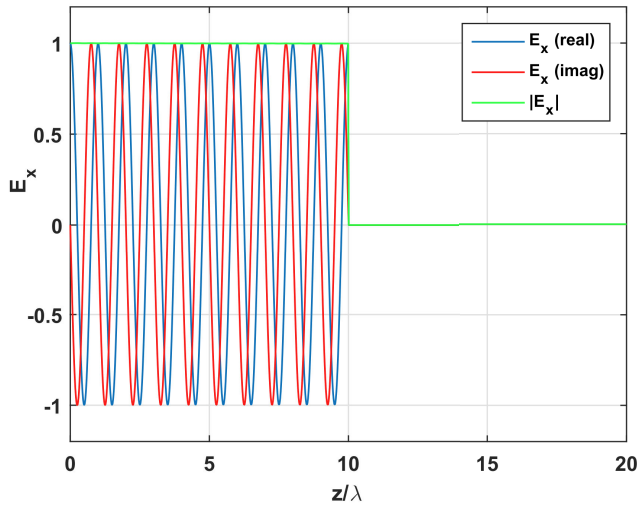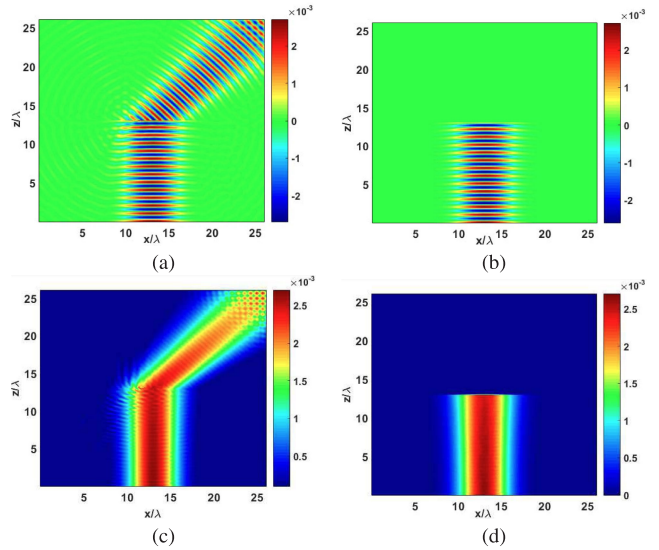
FIGURE 17. The simulation results of a fully absorbing metasurface calculated according to 1-D FEM-GSTC in [53]. The metasurface is situated at $z = 10\lambda$, where a plane wave with an electric field magnitude of 1 V/m approaches from the left [53].

FIGURE 18. The simulation results display the (a), (b) real part of Hy, and (c), (d) magnitude part of Hy for a (a), (c) 45° refracted metasurface, and (b), (d) fully absorbing metasurface [53]. The calculations were performed by a 2-D FEM-GSTC numerical modeling, as outlined in [53]. Noted that the designed metasurface is positioned at $z = 13\lambda$ with dimensions of 10λ along the x-axis, where a normal plane wave impinges from below [53].

the synthesis process introduce slight discrepancies between calculated values and full-wave simulation results [88]. Nonetheless, these simplifications significantly facilitate the design of a metasurface with the desired performance. Cell dimensions were fine-tuned and optimized, resulting in $l = 15$ mm and $r_1 = 9$ mm [34], [87], [88].

C. SYNTHESIZING A METASURFACE STRUCTURE WITH SUSCEPTIBILITY MODELING OF GSTCS

In this subsection, we review some simulation results based on synthesizing of metasurface with susceptibility approach discussed in detail in [53]. Different GSTCs modelling approaches using finite element methods and finite difference techniques are presented in [53] and [54], respectively, which can be suitable for solving EM engineering problems. The numerical method of FEM in [53] allows the modeling of complex geometries, facilitating adaptability with the well-known tetrahedral meshing process. Currently, commercial full-wave simulators can model various boundary conditions, including the perfectly matched layer (PML), perfect electric conductor (PEC), periodic boundary condition, radiation boundary condition, and perfect magnetic conductor (PMC) [12]. As already mentioned, there has not been any commercial simulation tool capable of incorporating GSTCs [50], [51]. The importance of these numerical method examples lies in paving the way for further research in developing GSTCs modeling for designing various metasurface applications with shorter simulation times [50], [51].

In [53], the authors initially modeled a perfect absorber in a one-dimensional scenario using finite element methods. In this case, the values of transmitted and reflected fields are set to zero in (79) and (80), resulting in susceptibility values of $\chi_{xx}^{ee} = \chi_{yy}^{mm} = 2/jk_0$. As shown in Fig. 17 [53],

the real and imaginary parts of the incident electric field are observed on the left side, while there is no transmitted field on the right side of the metasurface located at the center of the computational line domain [53]. It is worth noting that if a reflective wave existed on the left side, it would create a standing wave with a different amplitude [53].

$$\chi_{ee}^{xx} = \frac{2}{j\omega\varepsilon_0}\left[\frac{H_y^{inc} + H_y^{ref} - H_y^{tr}}{E_x^{inc} + E_x^{ref} + E_x^{tr}}\right] \quad (79)$$

$$\chi_{mm}^{yy} = \frac{2}{j\omega\mu_0}\left[\frac{E_x^{inc} + E_x^{ref} - E_x^{tr}}{H_y^{inc} + H_y^{ref} + H_y^{tr}}\right] \quad (80)$$

In addition, a two-dimensional scenario is explored in [53] using a computational domain of 26λ by 26λ, with the designed reflectionless metasurface located at 13λ. A normal incident plane wave with a Gaussian profile impinges on the metasurface from below, as shown in Fig. 18. The angle of the transmitted wave is set at 45° relative to the metasurface plane [53]. Based on the finite element method incorporating GSTCs [53], the numerical simulation results are displayed in Fig. 18. A pattern of standing waves can be observed in the top-right corner of Fig. 18(a) and Fig. 18(c). The authors in [53] explained that this phenomenon occurred due to their utilization of the first-order Absorbing Boundary Condition (ABC), which led to reflections from the absorbing boundary of the computational domain [53]. In practice, deploying a perfectly matched layer (PML) or the second-order ABC would help minimize this standing wave [53], [90]. Furthermore, another example of this numerical modeling approach is employed for synthesizing a two-dimensional perfect absorber, and the results are depicted in Fig. 18 (b) and Fig. 18 (d).
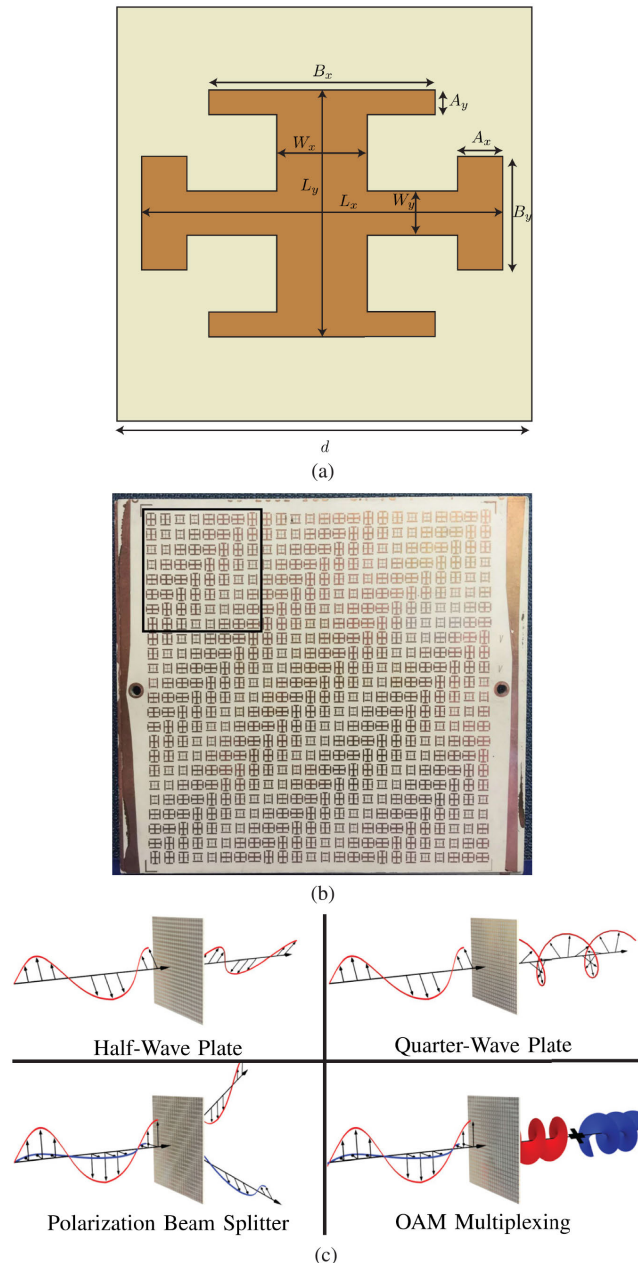
FIGURE 19. (a) A conventional metallic layer of unit cell which is parametrized for designing various metasurface structures based on GSTCs approaches, (b) A metasurface prototype that functions as a polarization beam splitter, constructed with a specific arrangement of various designed cells obtained from the parametrized cell in (a) through GSTC methodologies, and (c) images showing the functionality of the four fabricated metasurfaces designed using GSTC synthesis methods: a half-wave plate, a quarter-wave plate, a polarization beam splitter, and an orbital angular momentum multiplexing metasurface structure. Reprinted from [90], with the permission of AIP Publishing.

Finally, it is worth noting that metasurfaces have seen recent advancements in synthesis, design, and deployment across various applications [91], [92], [93], [94], [95], [96], [97], [98], [99], utilizing transient boundary conditions. Fig. 19 shows some examples of designed metasurface structures with a desired functionality [90], such as a half-wave plate, a quarter-wave plate, a polarization beam splitter,

and an orbital angular momentum multiplexing metasurface structure. This figure showcases different metasurface samples that were fabricated using GSTCs modeling approaches. For further information, interested readers can refer to [90].

VIII. CONCLUSION

In order to demonstrate how conventional Maxwell's boundary conditions are converted to the GSTCs, we have employed different physical presentations and justifications based on the induced dipole moments of simple scatters on the metasurface. In addition, we have shown different snapshots when the electric and magnetic fields touch the metasurface in the presence of magnetic and electric dipole moment responses. These electromagnetic responses have been expressed in terms of equivalent surface polarization and magnetization current densities and spatial tangential gradients of the normal surface polarization and magnetization densities. It has been deduced that both the normal and transverse components of the electric surface polarization density and the surface magnetization density must be involved in studying the most general case of the metasurface. We have reviewed several modeling approaches of the GSTCs, including polarizability, susceptibility, and impedance/admittance models, and discussed their interrelations. Then, we have developed these modeling forms of the GSTCs for designing bianisotropic metasurfaces. Finally, multiple examples to demonstrate the benefits of designing metasurfaces using GSTCs have been provided. We expect that this study may help open new paradigms for developing advanced metasurface modeling techniques and will be particularly useful for a convenient understanding of GSTCs requiring the presence of dipolar moment responses.

REFERENCES

[1] U. S. Inan and A. S. Inan, *Electromagnetics Waves*, 1st ed. Upper Saddle River, NJ, USA: Prentice-Hall, 2000.

[2] N. Engheta, "Metamaterials with high degrees of freedom: Space, time, and more," *Nanophotonics*, vol. 10, no. 1, pp. 639–642, Oct. 2020.

[3] N. Engheta and R. W. Ziolkowski, *Metamaterials: Physics and Engineering Explorations*. Hoboken, NJ, USA: Wiley, 2006.

[4] K. Achouri and C. Caloz, *Electromagnetic Metasurfaces: Theory and Applications*. Hoboken, NJ, USA: Wiley, 2021.

[5] M. H. Mostafa, M. S. Mirmoosa, M. S. Sidorenko, V. S. Asadchy, and S. A. Tretyakov, "Temporal interfaces in complex electromagnetic materials: An overview," *Opt. Mater. Exp.*, vol. 14, no. 5, p. 1103, May 2024.

[6] A. Ghaneizadeh, K. Mafinezhad, and M. Joodaki, "A new compact dual-band perfect absorption ultrathin planar metasurface energy harvester in X- and V-bands with a wide incident angle," *AIP Adv.*, vol. 10, no. 8, Aug. 2020, Art. no. 085007, doi: 10.1063/5.0012857.

[7] N. Yu and F. Capasso, "Flat optics with designer metasurfaces," *Nature Mater.*, vol. 13, no. 2, pp. 139–150, Feb. 2014.

[8] A. Ghaneizadeh, K. Mafinezhad, and M. Joodaki, "An extremely ultrathin flexible Huygens's transformer," *AIP Adv.*, vol. 10, no. 10, Oct. 2020, Art. no. 105201, doi: 10.1063/5.0016373.

[9] K. Achouri and C. Caloz, "Design, concepts, and applications of electromagnetic metasurfaces," *Nanophotonics*, vol. 7, no. 6, pp. 1095–1116, Jun. 2018, doi: 10.1515/nanoph-2017-0119.

[10] C. Caloz, "Tomorrow's metamaterials: Manipulation of electromagnetic waves in space, time and spacetime," 2016, *arXiv:1602.04340*.

[11] S. B. Glybovski, S. A. Tretyakov, P. A. Belov, Y. S. Kivshar, and C. R. Simovski, "Metasurfaces: From microwaves to visible," *Phys. Rep.*, vol. 634, pp. 1–72, May 2016.

[12] Y. Vahabzadeh, N. Chamanara, K. Achouri, and C. Caloz, "Computational analysis of metasurfaces," *IEEE J. Multiscale Multiphys. Comput. Techn.*, vol. 3, pp. 37–49, 2018.

[13] C. L. Holloway, E. F. Kuester, J. A. Gordon, J. O'Hara, J. Booth, and D. R. Smith, "An overview of the theory and applications of metasurfaces: The two-dimensional equivalents of metamaterials," *IEEE Antennas Propag. Mag.*, vol. 54, no. 2, pp. 10–35, Apr. 2012.

[14] Y. Huang, J. Luo, M. Pu, Y. Guo, Z. Zhao, X. Ma, X. Li, and X. Luo, "Catenary electromagnetics for ultra-broadband lightweight absorbers and large-scale flat antennas," *Adv. Sci.*, vol. 6, no. 7, Apr. 2019, Art. no. 1801691.

[15] K. Achouri and O. J. F. Martin, "Extension of Lorentz reciprocity and Poynting theorems for spatially dispersive media with quadrupolar responses," *Phys. Rev. B*, vol. 104, no. 16, Oct. 2021, Art. no. 165426.

[16] E. F. Kuester, M. A. Mohamed, M. Piket-May, and C. L. Holloway, "Averaged transition conditions for electromagnetic fields at a metafilm," *IEEE Trans. Antennas Propag.*, vol. 51, no. 10, pp. 2641–2651, Oct. 2003.

[17] C. L. Holloway, A. Dienstfrey, E. F. Kuester, J. F. O'Hara, A. K. Azad, and A. J. Taylor, "A discussion on the interpretation and characterization of metafilms/metasurfaces: The two-dimensional equivalent of metamaterials," *Metamaterials*, vol. 3, no. 2, pp. 100–112, Oct. 2009.

[18] M. Kavehrad, "Multi-band multi-service sensing: Metamaterials myth and reality," in *SPIE Proc.*, Dec. 2013.

[19] M. Chen, "Design and applications of printed-circuit-board Huygens' metasurfaces," Ph.D. dissertation, Dept. Elect. Comput. Eng., Univ. Toronto, Ontario, Canada, 2021.

[20] G. Lavigne, T. Kodera, and C. Caloz, "Metasurface magnetless specular isolator," *Sci. Rep.*, vol. 12, no. 1, Apr. 2022, Art. no. 5652.

[21] A. Ghaneizadeh, K. Mafinezhad, and M. Joodaki, "Design and fabrication of a 2D-isotropic flexible ultra-thin metasurface for ambient electromagnetic energy harvesting," *AIP Adv.*, vol. 9, no. 2, Feb. 2019, Art. no. 025304.

[22] M. E. Badawe, T. S. Almoneef, and O. M. Ramahi, "A true metasurface antenna," *Sci. Rep.*, vol. 6, no. 1, Jan. 2016, Art. no. 19268.

[23] C. Huang, S. Hu, G. C. Alexandropoulos, A. Zappone, C. Yuen, R. Zhang, M. D. Renzo, and M. Debbah, "Holographic MIMO surfaces for 6G wireless networks: Opportunities, challenges, and trends," *IEEE Wireless Commun.*, vol. 27, no. 5, pp. 118–125, Oct. 2020.

[24] C. Zeng, H. Lu, D. Mao, Y. Du, H. Hua, W. Zhao, and J. Zhao, "Graphene-empowered dynamic metasurfaces and metadevices," *Opto-Electronic Adv.*, vol. 5, no. 4, 2022, Art. no. 200098.

[25] A. S. Solntsev, G. S. Agarwal, and Y. S. Kivshar, "Metasurfaces for quantum photonics," *Nature Photon.*, vol. 15, no. 5, pp. 327–336, Apr. 2021.

[26] A. Vaskin, R. Kolkowski, A. F. Koenderink, and I. Staude, "Light-emitting metasurfaces," *Nanophotonics*, vol. 8, no. 7, pp. 1151–1198, Jul. 2019, doi: 10.1515/nanoph-2019-0110.

[27] A. Li, S. Singh, and D. Sievenpiper, "Metasurfaces and their applications," *Nanophotonics*, vol. 7, no. 6, 2018, Art. no. 9891011.

[28] V. G. Ataloglou, M. Chen, M. Kim, and G. V. Eleftheriades, "Microwave Huygens' metasurfaces: Fundamentals and applications," *IEEE J. Microw.*, vol. 1, no. 1, pp. 374–388, Jan. 2021.

[29] X. Chen, T. M. Grzegorczyk, B.-I. Wu, J. Pacheco, and J. A. Kong, "Robust method to retrieve the constitutive effective parameters of metamaterials," *Phys. Rev. E, Stat. Phys. Plasmas Fluids Relat. Interdiscip. Top.*, vol. 70, no. 1, Jul. 2004, Art. no. 016608.

[30] D. R. Smith, D. C. Vier, T. Koschny, and C. M. Soukoulis, "Electromagnetic parameter retrieval from inhomogeneous metamaterials," *Phys. Rev. E, Stat. Phys. Plasmas Fluids Relat. Interdiscip. Top.*, vol. 71, Mar. 2005, Art. no. 036617.

[31] C. A. Balanis, "Antenna theory: A review," *Proc. IEEE*, vol. 80, no. 1, pp. 7–23, 1992.

[32] A. Ghaneizadeh, M. Joodaki, J. Börcsök, A. Golmakani, and K. Mafinezhad, "Analysis, design, and implementation of a new extremely ultrathin 2-D-Isotropic flexible energy harvester using symmetric patch FSS," *IEEE Trans. Microw. Theory Techn.*, vol. 68, no. 6, pp. 2108–2115, Jun. 2020.

[33] T. H. Nguyen and G. Byun, "A suboptimal approach to Huygens' metasurfaces for wide-angle refraction," *IEEE Trans. Microw. Theory Techn.*, vol. 70, no. 5, pp. 2588–2598, May 2022.

[34] T. Niemi, A. O. Karilainen, and S. A. Tretyakov, "Synthesis of polarization transformers," *IEEE Trans. Antennas Propag.*, vol. 61, no. 6, pp. 3102–3111, Jun. 2013.

[35] A. Mehdipour, J. W. Wong, and G. V. Eleftheriades, "Beam-squinting reduction of leaky-wave antennas using Huygens metasurfaces," *IEEE Trans. Antennas Propag.*, vol. 63, no. 3, pp. 978–992, Mar. 2015.

[36] R. M. H. Bilal, M. A. Baqir, P. K. Choudhury, M. Karaaslan, M. M. Ali, O. Altlntas, A. A. Rahim, E. Unal, and C. Sabah, "Wideband microwave absorber comprising metallic split-ring resonators surrounded with E-shaped fractal metamaterial," *IEEE Access*, vol. 9, pp. 5670–5677, 2021, doi: 10.1109/ACCESS.2020.3048927.

[37] V. S. Asadchy, Y. Ra'di, J. Vehmas, and S. A. Tretyakov, "Functional metamirrors using bianisotropic elements," *Phys. Rev. Lett.*, vol. 114, no. 9, Mar. 2015, Art. no. 095503, doi: 10.1103/physrevlett.114.095503.

[38] V. S. Asadchy, I. A. Faniayeu, Y. Ra'di, S. A. Khakhomov, I. V. Semchenko, and S. A. Tretyakov, "Broadband reflectionless metasheets: Frequency-selective transmission and perfect absorption," *Phys. Rev. X*, vol. 5, no. 3, Jul. 2015, Art. no. 031005.

[39] M. Selvanayagam and G. V. Eleftheriades, "Design and measurement of tensor impedance transmitarrays for chiral polarization control," *IEEE Trans. Microw. Theory Techn.*, vol. 64, no. 2, pp. 414–428, Feb. 2016.

[40] C. Pfeiffer and A. Grbic, "Millimeter-wave transmitarrays for wavefront and polarization control," *IEEE Trans. Microw. Theory Techn.*, vol. 61, no. 12, pp. 4407–4417, Dec. 2013.

[41] M. Zhang, M. Pu, F. Zhang, Y. Guo, Q. He, X. Ma, Y. Huang, X. Li, H. Yu, and X. Luo, "Plasmonic metasurfaces for switchable photonic spin–orbit interactions based on phase change materials," *Adv. Sci.*, vol. 5, no. 10, Oct. 2018, Art. no. 1800835, doi: 10.1002/advs.201800835.

[42] W. Yao, L. Tang, J. Wang, C. Ji, X. Wei, and Y. Jiang, "Spectrally and spatially tunable terahertz metasurface lens based on graphene surface plasmons," *IEEE Photon. J.*, vol. 10, no. 4, pp. 1–8, Aug. 2018.

[43] Z. Yue, J. Li, J. Li, C. Zheng, J. Liu, G. Wang, H. Xu, M. Chen, Y. Zhang, Y. Zhang, and J. Yao, "Terahertz metasurface zone plates with arbitrary polarizations to a fixed polarization conversion," *Opto-Electron. Sci.*, vol. 1, no. 3, 2022, Art. no. 210014, doi: 10.29026/oes.2022.210014.

[44] H. Kocer, A. Ozer, S. Butun, K. Wang, J. Wu, H. Kurt, and K. Aydin, "Thermally tuning infrared light scattering using planar layered thin films and space gradient metasurface," *IEEE J. Sel. Topics Quantum Electron.*, vol. 25, no. 3, pp. 1–7, May 2019, doi: 10.1109/JSTQE.2019.2900607.

[45] Y. Guo, S. Zhang, M. Pu, Q. He, J. Jin, M. Xu, Y. Zhang, P. Gao, and X. Luo, "Spin-decoupled metasurface for simultaneous detection of spin and orbital angular momenta via momentum transformation," *Light, Sci. Appl.*, vol. 10, no. 1, pp. 1–15, Mar. 2021.

[46] Y. Zhu, X. Chen, W. Yuan, Z. Chu, K.-Y. Wong, D. Lei, and Y. Yu, "A waveguide metasurface based quasi-far-field transverse-electric superlens," *Opto-Electron. Adv.*, vol. 4, no. 10, 2021, Art. no. 210013, doi: 10.29026/oea.2021.210013.

[47] C. Caloz and Z.-L. Deck-Léger, "Spacetime metamaterials," 2019, *arXiv:1905.00560*.

[48] F. Yang and Y. Rahmat-Samii, *Surface Electromagnetics: With Applications in Antenna, Microwave, and Optical Engineering*, 1st ed. Cambridge, U.K.: Cambridge Univ. Press, 2019.

[49] C. L. Holloway and E. F. Kuester, "Generalized sheet transition conditions for a metascreenA fishnet metasurface," *IEEE Trans. Antennas Propag.*, vol. 66, no. 5, Oct. 2018, Art. no. 24142427.

[50] S. Tian, K. Wu, and Q. Ren, "Modeling of metasurfaces using discontinuous Galerkin time-domain method based on generalized sheet transition conditions," *IEEE Trans. Antennas Propag.*, vol. 70, no. 8, pp. 6905–6917, Aug. 2022.

[51] K. Wu, S. Tian, and Q. Ren, "A vectorial discontinuous Galerkin time-domain method incorporating generalized sheet transition conditions," *IEEE Trans. Microw. Theory Techn.*, vol. 70, no. 8, pp. 3765–3775, Aug. 2022.

[52] Y. Vahabzadeh, N. Chamanara, and C. Caloz, "Generalized sheet transition condition FDTD simulation of metasurface," *IEEE Trans. Antennas Propag.*, vol. 66, no. 1, pp. 271–280, Jan. 2018.

[53] S. Sandeep, J.-M. Jin, and C. Caloz, "Finite-element modeling of metasurfaces with generalized sheet transition conditions," *IEEE Trans. Antennas Propag.*, vol. 65, no. 5, pp. 2413–2420, May 2017.

[54] Y. Vahabzadeh, K. Achouri, and C. Caloz, "Simulation of metasurfaces in finite difference techniques," *IEEE Trans. Antennas Propag.*, vol. 64, no. 11, pp. 4753–4759, Nov. 2016.

[55] N. Chamanara, K. Achouri, and C. Caloz, "Efficient analysis of metasurfaces in terms of spectral-domain GSTC integral equations," *IEEE Trans. Antennas Propag.*, vol. 65, no. 10, pp. 5340–5347, Oct. 2017.

[56] K. Wang, J.-J. Laurin, Q. Zhang, M. A. M. Hassan, Q. Zhang, and K. Wu, "Simulation of cylindrical metasurfaces using GSTC-MFCM," *IEEE Trans. Antennas Propag.*, vol. 69, no. 1, pp. 263–272, Jan. 2021.

[57] S. Sandeep and S. Y. Huang, "Simulation of circular cylindrical meta-surfaces using GSTC-MoM," *IEEE J. Multiscale Multiphys. Comput. Techn.*, vol. 3, pp. 1–192, 2018, Art. no. 185192.

[58] J. Budhu and A. Grbic, "Recent advances in bianisotropic bound-ary conditions: Theory, capabilities, realizations, and applications," *Nanophotonics*, vol. 10, no. 16, pp. 4075–4112, Nov. 2021.

[59] S. Ramo, J. R. Whinnery, and T. V. Duzer, *Fields and Waves in Communication Electronics*, 3rd ed. Hoboken, NJ, USA: Wiley, 1994.

[60] V. S. Asadchy, A. Díaz-Rubio, and S. A. Tretyakov, "Bianisotropic metasurfaces: Physics and applications," *Nanophotonics*, vol. 7, no. 6, pp. 1069–1094, Jun. 2018.

[61] K. Achouri, M. A. Salem, and C. Caloz, "General metasurface synthesis based on susceptibility tensors," *IEEE Trans. Antennas Propag.*, vol. 63, no. 7, pp. 2977–2991, Jul. 2015.

[62] J. G. V. Bladel, *Electromagnetic Fields*. Hoboken, NJ, USA: Wiley, 2007.

[63] J. D. Kraus and K. R. Carver, *Electromagnetics*, 2nd ed. New York, NY, USA: McGraw-Hill, 1973.

[64] D. H. Staelin, *Electromagnetics and Application*. Cambridge, MA, USA: MIT Press, 2011.

[65] S. Tretyakov, *Analytical Modeling in Applied Electromagnetics*. Norwood, MA, USA: Artech House, 2003.

[66] M. Dehmollaian, Y. Vahabzadeh, K. Achouri, and C. Caloz, "Limitations of the metasurface diluted-slab model," *IEEE J. Multiscale Multiphys. Comput. Techn.*, vol. 5, pp. 255–264, 2020.

[67] A. Epstein and G. V. Eleftheriades, "Huygens' metasurfaces via the equivalence principle: Design and applications," *J. Opt. Soc. Amer. B, Opt. Phys.*, vol. 33, no. 2, Feb. 2016, Art. no. A31A50, doi: 10.1364/josab.33.000a31.

[68] Z. Wang, J. Liu, X. Ding, W. Zhao, K. Zhang, H. Li, B. Ratni, S. N. Burokur, and Q. Wu, "Three-dimensional microwave holography based on broadband Huygens' metasurface," *Phys. Rev. Appl.*, vol. 13, no. 1, Jan. 2020, Art. no. 014033.

[69] Y. Ra'di, C. R. Simovski, and S. A. Tretyakov, "Thin perfect absorbers for electromagnetic waves: Theory, design, and realizations," *Phys. Rev. Appl.*, vol. 3, no. 3, Mar. 2015, Art. no. 037001.

[70] N. Yu, P. Genevet, M. A. Kats, F. Aieta, J.-P. Tetienne, F. Capasso, and Z. Gaburro, "Light propagation with phase discontinuities: Generalized laws of reflection and refraction," *Science*, vol. 334, no. 6054, pp. 333–337, Oct. 2011.

[71] M. Koohestani and A. Ghaneizadeh, "An ultra-thin double-functional metasurface patch antenna for UHF RFID applications," *Sci. Rep.*, vol. 11, no. 1, Jan. 2021, Art. no. 857.

[72] M. M. Idemen, *Discontinuities in the Electromagnetic Field*. Hoboken, NJ, USA: Wiley, 2011.

[73] X.-X. Liu, Y. Zhao, and A. Alù, "Polarizability tensor retrieval for subwavelength particles of arbitrary shape," *IEEE Trans. Antennas Propag.*, vol. 64, no. 6, pp. 2301–2310, Jun. 2016.

[74] C. Pfeiffer and A. Grbic, "Metamaterial Huygens' surfaces: Tailoring wave fronts with reflectionless sheets," *Phys. Rev. Lett.*, vol. 110, no. 19, May 2013, Art. no. 197401.

[75] M. Selvanayagam and G. V. Eleftheriades, "Discontinuous electromag-netic fields using orthogonal electric and magnetic currents for wavefront manipulation," *Opt. Exp.*, vol. 21, no. 12, p. 14409, Jun. 2013.

[76] M. Chen, E. Abdo-Sánchez, A. Epstein, and G. V. Eleftheriades, "Theory, design, and experimental verification of a reflectionless bianisotropic Huygens' metasurface for wide-angle refraction," *Phys. Rev. B*, vol. 97, no. 12, Mar. 2018, Art. no. 125433.

[77] J. W. Wu, Z. X. Wang, R. Y. Wu, H. Xu, Q. Cheng, and T. J. Cui, "Simple and comprehensive strategy to synthesize Huygens metasurface antenna and verification," *IEEE Trans. Antennas Propag.*, vol. 71, no. 8, Apr. 2023, Art. no. 66526666.

[78] C. L. Holloway, M. A. Mohamed, E. F. Kuester, and A. Dienstfrey, "Reflection and transmission properties of a metafilm: With an application to a controllable surface composed of resonant particles," *IEEE Trans. Electromagn. Compat.*, vol. 47, no. 4, pp. 853–865, Nov. 2005.

[79] J. P. S. Wong, M. Selvanayagam, and G. V. Eleftheriades, "Polarization considerations for scalar Huygens metasurfaces and characterization for 2-D refraction," *IEEE Trans. Microw. Theory Techn.*, vol. 63, no. 3, pp. 913–924, Mar. 2015.

[80] T. B. A. Senior and J. L. Volakis, *Approximate Boundary Conditions in Electromagnetics*. London, U.K.: Inst. Elect. Eng., 1995.

[81] K. Achouri, Y. Vahabzadeh, and C. Caloz, "Mathematical synthesis and analysis of a second-order magneto-electrically nonlinear metasurface," *Opt. Exp.*, vol. 25, no. 16, p. 19013, Aug. 2017.

[82] C. Pfeiffer and A. Grbic, "Bianisotropic metasurfaces for optimal polarization control: Analysis and synthesis," *Phys. Rev. Appl.*, vol. 2, no. 4, Oct. 2014, Art. no. 044011.

[83] Y. Ra'di, V. S. Asadchy, and S. A. Tretyakov, "Total absorption of electromagnetic waves in ultimately thin layers," *IEEE Trans. Antennas Propag.*, vol. 61, no. 9, pp. 4606–4614, Sep. 2013.

[84] M. Dehmollaian, G. Lavigne, and C. Caloz, "Comparison of tensor boundary conditions with generalized sheet transition conditions," *IEEE Trans. Antennas Propag.*, vol. 67, no. 12, pp. 7396–7406, Dec. 2019.

[85] V. S. Asadchy, M. Albooyeh, S. N. Tcvetkova, A. Díaz-Rubio, Y. Ra'di, and S. A. Tretyakov, "Perfect control of reflection and refraction using spatially dispersive metasurfaces," *Phys. Rev. B*, vol. 94, no. 7, Aug. 2016, Art. no. 075142.

[86] A. Epstein and G. V. Eleftheriades, "Arbitrary power-conserving field transformations with passive lossless omega-type bianisotropic metasur-faces," *IEEE Trans. Antennas Propag.*, vol. 64, no. 9, pp. 3880–3895, Sep. 2016.

[87] T. Niemi, A. O. Karilainen, and S. A. Tretyakov, "Synthesizing a twist polarizer," in *Proc. IEEE Int. Symp. Antennas Propag.*, Jul. 2012, pp. 1–2, doi: 10.1109/APS.2012.6349202.

[88] T. Niemi. (2012). *Polarization Transformations in Bianisotropic Arrays*. [Online]. Available: https://aaltodoc.aalto.fi/server/api/core/bitstreams/3b52864c-c813-4e97-8b31-d9292de5114d/content

[89] V. V. Yatsenko, S. I. Maslovski, S. A. Tretyakov, S. L. Prosvirnin, and S. Zouhdi, "Plane-wave reflection from double arrays of small magnetoelectric scatterers," *IEEE Trans. Antennas Propag.*, vol. 51, no. 1, pp. 2–11, Jan. 2003.

[90] K. Achouri, G. Lavigne, and C. Caloz, "Comparison of two synthesis methods for birefringent metasurfaces," *J. Appl. Phys.*, vol. 120, no. 23, Dec. 2016, Art. no. 235305, doi: 10.1063/1.4972195.

[91] J. G. N. Rahmeier, J. Dugan, T. J. Smy, and S. Gupta, "Time-domain analysis of temporally and spatially dispersive metasurfaces in GSTC-FDTD frameworks," *IEEE Access*, vol. 12, pp. 22557–22572, 2024.

[92] J. Dugan, J. G. N. Rahmeier, T. J. Smy, and S. Gupta, "Spatially dispersive metasurfaces—Part III: Zero-thickness modeling of periodic and finite nonuniform surfaces," *IEEE Trans. Antennas Propag.*, vol. 71, no. 7, pp. 5935–5945, Jul. 2023.

[93] T. J. Smy and S. Gupta, "Eigenfunction expansion (EFE) analysis of cylindrical metasurfaces—Part II: Sectors and multishells," *IEEE Trans. Microw. Theory Techn.*, vol. 71, no. 8, pp. 3366–3378, Aug. 2023, doi: 10.1109/TMTT.2023.3240418.

[94] G. Cai, X. Liu, T. Shen, J. Liu, N. Liu, and Q. H. Liu, "A full-vectorial spectral element method with generalized sheet transition conditions for high-efficiency metasurface/metafilm simulation," *IEEE Trans. Antennas Propag.*, vol. 71, no. 3, pp. 2652–2660, Mar. 2023.

[95] L. Chen, M. B. Özakin, R. Zhao, and H. Bagci, "A locally-implicit discontinuous Galerkin time-domain method to simulate metasurfaces using generalized sheet transition conditions," *IEEE Trans. Antennas Propag.*, vol. 71, no. 1, pp. 869–881, Jan. 2023.

[96] T. J. Smy, J. G. N. Rahmeier, J. Dugan, and S. Gupta, "Spatially dispersive metasurfacespart II: IE-GSTC-SD field solver with extended GSTCs," *IEEE Trans. Antennas Propag.*, vol. 71, no. 7, pp. 5920–5934, Jul. 2023.

[97] J. Dugan, T. J. Smy, and S. Gupta, "Accelerated IE-GSTC solver for large-scale metasurface field scattering problems using fast multipole method (FMM)," *IEEE Trans. Antennas Propag.*, vol. 70, no. 10, pp. 9524–9533, Oct. 2022.

[98] K. Hosseini and Z. Atlasbaf, "PLRC-FDTD modeling of general GSTC-based dispersive bianisotropic metasurfaces," *IEEE Trans. Antennas Propag.*, vol. 66, no. 1, pp. 262–270, Jan. 2018.

[99] T. J. Smy, S. A. Stewart, and S. Gupta, "Surface susceptibility synthesis of metasurface holograms for creating electromagnetic illusions," *IEEE Access*, vol. 8, pp. 93408–93425, 2020.

ALIREZA GHANEIZADEH received the B.Sc. degree in electrical engineering from the Shahid Bahonar University of Kerman, Kerman, Iran, in 2012, the M.Sc. degree in electrical engineering from the University of Sistan and Baluchestan, Zahedan, Iran, in 2015 and the Ph.D. degree in electrical engineering from the Sadjad University of Technology, Mashhad, Iran, in 2020. He is currently a Postdoctoral Fellow with the School of Computer Science and Engineering, Constructor University (former Jacobs University), Bremen, Germany. He has authored and coauthored more than ten scientific contributions in peer-reviewed conferences and journals. His research interests include wave physics and engineering, mostly focusing on electromagnetic metasurface structures.

MOJTABA JOODAKI (Senior Member, IEEE) received the B.Sc. degree in electrical and electronic engineering from Iran Science and Technology University, Tehran, Iran, in 1994, the M.Sc. degree in electrical and electronic engineering from Tarbiat Modarres University, Tehran, in 1997, and the Ph.D. degree in electrical engineering from Kassel University, Kassel, Germany, in 2002. He joined ATMEL Germany GmbH, Heilbronn, Germany, as a Device Engineer, in 2002, where he was working on technology development, modeling, and characterization of Si- and SiGe-based devices for RF applications. In April 2005, he joined Infineon Technologies AG, Munich, Germany, as a Development Engineer, where he was responsible for electromagnetic interference (EMI)/electromagnetic compatibility (EMC) of memory modules. In his last industrial position, from October 2006 to July 2009, he was a Device Engineer with Qimonda GmbH, Dresden, Germany, involved in developing nanotransistors for dynamic random access memory (DRAM) products. Then, he started working as a Visiting Scientist and a Lecturer with the Institute of Nanostructure Technologies and Analytics (INA), Kassel University, where he defended his Habilitation dissertation in April 2011. In 2010, he joined the Department of Electrical Engineering, Ferdowsi University of Mashhad, Mashhad, Iran, as an Assistant Professor of Electronic Engineering (RF Circuit Design and Semiconductor Devices and Technology), where he was promoted to an Associate Professor in September 2011 and a Professor in July 2018. Since January 2020, he has been with Constructor University (former Jacobs University), Bremen, Germany, as a Professor of Electrical Engineering and Electrical, and the Computer Engineering Program Chair. His research interests include modeling, characterization, and fabrication of nanodevices (organic and inorganic) for memory, high-frequency, and optoelectronic applications and EMC of electronic products. He is a Life Member of the International Society for Optics and Photonics (SPIE). He has been awarded several prizes for his scientific activities, including the Best Dissertation Prize of North Hessen Universities from the Association of German Engineers (VDI) in 2004, the Young Graduated Research Fellowship of the Gallium Arsenide (GaAs) Association in the European Microwave Week 2001 and 2002, and the F-MadeScholarship of SPIE 2002.

● ● ●